The Landsat Scale Break in Stratocumulus as a Three-Dimensional Radiative Transfer Effect: Implications for Cloud Remote Sensing

Anthony Davis,* Alexander Marshak,* Robert Cahalan, and Warren Wiscombe

Climate and Radiation Branch, NASA/Goddard Space Flight Center, Greenbelt, Maryland

ABSTRACT

Several studies have uncovered a break in the scaling properties of Landsat cloud scenes at nonabsorbing wavelengths. For scales greater than 200–400 m, the wavenumber spectrum is approximately power law in $k^{-5/3}$, but from there down to the smallest observable scales (50–100 m) follows another $k^{-\beta}$ law with $\beta > 3$. This implies very smooth radiance fields. The authors reexamine the empirical evidence for this scale break and explain it using fractal cloud models, Monte Carlo simulations, and a Green function approach to multiple scattering theory. In particular, the authors define the "radiative smoothing scale" and relate it to the characteristic scale of horizontal photon transport. The scale break was originally thought to occur at a scale commensurate with either the geometrical thickness Δ_z of the cloud, or with the "transport" mean free path $l_t = [(1 - g)\sigma]^{-1}$, which incorporates the effect of forward scattering (σ is extinction and g the asymmetry factor of the phase function). The smoothing scale is found to be approximately $\sqrt{l_t \Delta_z}$ at cloud top; this is the prediction of diffusion theory which applies when $(1 - g)\tau = \Delta_z/l_t \gtrsim 1$ (τ is optical thickness). Since the scale break is a tangible effect of net horizontal radiative fluxes excited by the fluctuations of τ, the smoothing scale sets an absolute lower bound on the range where one can neglect these fluxes and use plane-parallel theory locally, even for stratiform clouds. In particular, this constrains the retrieval of cloud properties from remotely sensed data. Finally, the characterization of horizontal photon transport suggests a new lidar technique for joint measurements of optical and geometrical thicknesses at about 0.5-km resolution.

1. Introduction and overview

Imagery from the Land Resources Satellite System (Landsat) has supplied the remote sensing community at large with a reliable cost-effective tool for studying the earth's environment over the past decades. Applications range from prospection geology to urban development and, in most cases, the occurrence of clouds in Landsat scenes is considered a nuisance. Recently, however, atmospheric scientists have developed a strong interest in this instrument. It is well calibrated and boasts unusually high spatial, spectral, and radiometric resolutions by meteorological standards:

- the five-channel Multi-Spectral Scanning (MSS, Landsat 1-3) radiometer resolved features at 80 m with 7 bits of dynamic range; and

- the seven-channel Thematic Mapper's (TM, Landsat 4-5) pixels are only 30 m wide and 8 bits deep.

Both instruments are almost linear in nadir-viewing radiance. Scores of Landsat completely or partially cloudy scenes have thus been acquired, mainly for the purposes of characterizing cloud morphology. One of the most remarkable properties of Landsat cloud scenes is their statistical "scale invariance:" quantities dependent on a scale parameter "r" follow power laws over a large range of values of r.

Two main types of scale-by-scale statistical analysis have been applied to cloudy Landsat data: joint area–perimeter distributions for ensembles of individual clouds, defined by some threshold in radiance or brightness temperature (Welch and Wielicki 1986; Welch et al. 1988; Cahalan and Joseph 1989; Sèze and Smith 1990), and spectral analysis of the 2D image (Cahalan and Snider 1989; Lovejoy et al. 1993; Barker and Davies 1992; Gollmer et al. 1994). We are primarily interested in the latter: wavenumber spectrum $E(k)$, which is essentially a scale-by-scale decomposition of variance as captured by Fourier modes, where the wavenumber $k = 1/r$ goes from $1/L$, L being the outer scale of the image, to the Nyquist frequency $1/(2\ell)$, ℓ being the pixel size. For Landsat radiance fields, $\ell = 30$ m (TM) or 80

*Additional affiliation: Science Systems and Applications, Inc., Lanham, Maryland.

Corresponding author address: Dr. Anthony Davis, Climate and Radiation Branch, NASA/Goddard Space Flight Center, Code 913, Greenbelt, MD 20771.
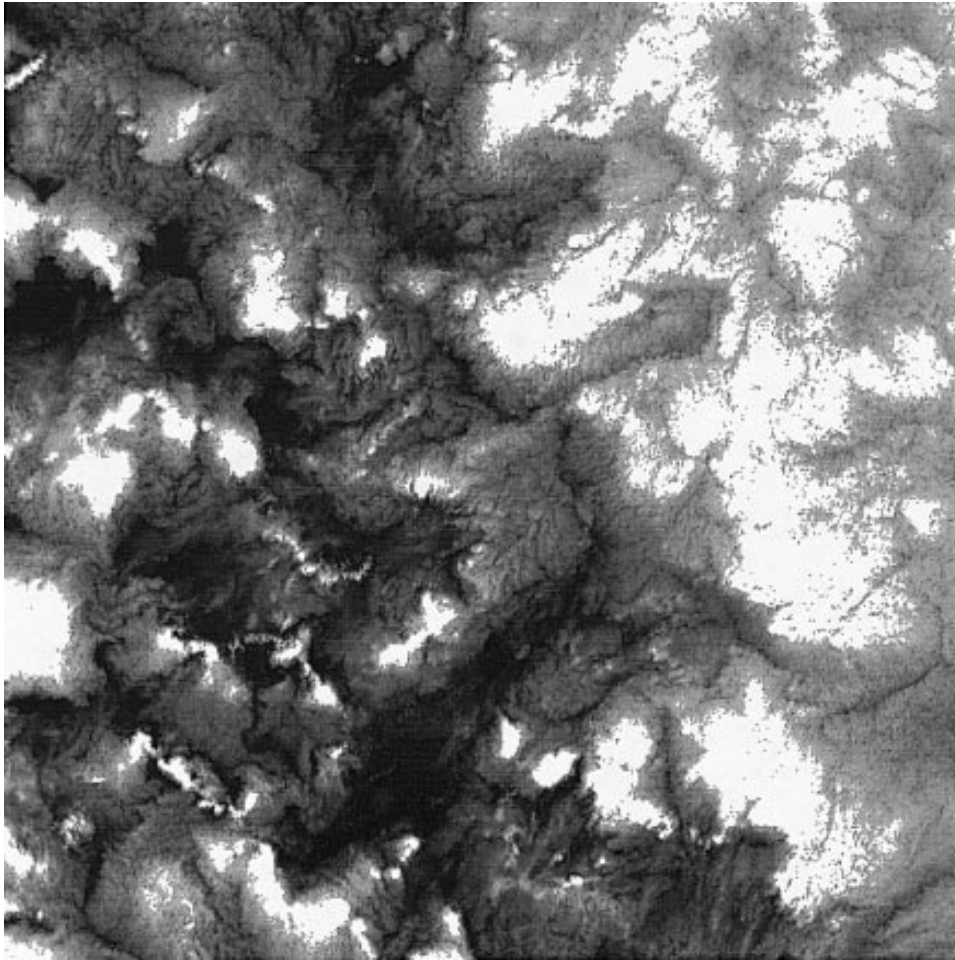E-mail: davis@climate.gsfc.nasa.gov

FIG. 1. Portion of a Landsat TM image in channel 2 (0.52–0.60 μm). This 123 km × 123 km scene was captured at $\ell = 30$ m resolution on 30 June 1987, off the coast of San Diego, California, during FIRE. These $4096^2 \approx 1.6 \times 10^7$ Landsat pixels show only a small portion of an extensive marine Sc deck. Some 17% of the pixels are saturated at gray level 255, mostly on the rhs.

m (MSS) and $E(k)$ is found to be approximately power law:

$$E(k) \sim k^{-\beta}, \tag{1}$$

with an exponent $\beta \approx 5/3$. However, this applies only over a subrange of k; at scales smaller than some critical scale, generally around 0.2–0.4 km, the spectrum becomes much steeper, with $\beta \gtrsim 3$ (Cahalan and Snider 1989).

In the following section, we survey the literature on the Landsat scale break and present new empirical evidence. In section 3, we present Monte Carlo simulations, scale break included, of Landsat-type radiometry based on randomly generated fractal cloud models (described and justified in the appendix). We also assess the sensitivity of the scale break to structural parameters of the models. By introducing the appropriate Green functions in section 4, we relate the scale break to horizontal photon transport in section 5 and use Brownian motion (photon diffusion) theory to explain this con-

nection. Applications to cloud property retrievals from both passive and active remote sensing methods are discussed in section 6 before being summarized in section 7.

2. The Landsat scale break

a. Observations

1) THE FOURIER-SPACE PICTURE

Figure 1 is a typical Landsat cloud scene, a 123 km × 123 km portion of a TM image, 4096^2 pixels (16 Mbytes of data). It was captured 30 June 1987, during the First ISCCP Regional Experiment (FIRE) off the coast of San Diego, California, and clearly illustrates the intricate structure of a marine stratocumulus (Sc) deck that extends far beyond this area.

Figure 2 shows an energy spectrum $E(k)$ plotted against scale $r = 1/k$ in log–log axes; the 2048 leftmost columns in Fig. 1 were used, thus avoiding the saturated
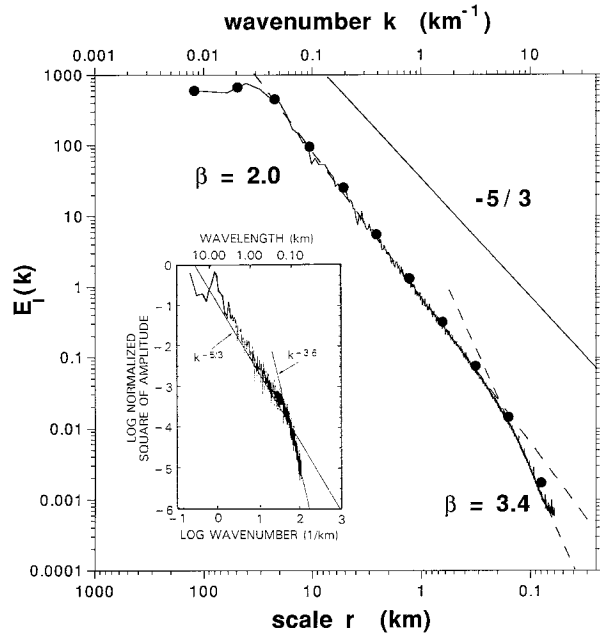
FIG. 2. Energy spectrum of half the radiance field in Fig. 1. To avoid saturation effects, only the lhs of the image is used where only 8% of the pixels have a value of 255; $E_i(k)$ was averaged over 2048 columns for $r = 1/k$ going from $2\ell = 60$ m to $L = 4096\ell \approx 123$ km. The scale break is clearly seen at $r \approx 200$ m. Digitization noise appears at the very smallest scales and at the expected level of $(1/48)/256^2 \approx 10^{-6.5}$ below the well-defined level of variance for the largest scales ($10^{-6.5}$; this is the variance of a deviate uniformly distributed between 0 and 0.5/256). The bold dots correspond to octavewide bins in k. A reference spectrum in $k^{-5/3}$ is indicated and the inset shows Cahalan and Snider's (1989) original figure showing a more noisy energy spectrum. Since it is based on only a few transepts through another Landsat image from the FIRE database.

regions on the rhs. By using over 8×10^6 data points, the statistical noise is low enough that we can see at least two distinct scale breaks: one at 0.2–0.4 km and one at $\approx$20 km. Between these two limits, power law behavior prevails with an exponent $\beta \approx 2$ in Eq. (1). For reference, a $\beta = 5/3$ law is shown on the same plot; this is the prediction of Corrsin's (1951) and Obukhov's (1949) phenomenology for a passive scalar in fully developed 3D turbulence, as well as Kraichnan's (1967) prediction for 2D turbulence.

The transition from $\beta \approx 2$ to $\beta \approx 0$ at 20 km marks the integral scale for marine Sc during FIRE and agrees with Davis et al.'s (1996a) estimate using in situ liquid water content (LWC) probings of the same type of cloud. This break is required on physical grounds to keep the overall variance finite, and because radiance is a nonnegative field the amplitude of its fluctuations cannot exceed its mean; simply put, the statistical significance of this break is that there are correlations in cloud structure up to 20 km and none above. However, Cahalan and Snider (1989) saw no flattening up to 100 km in their liquid water path (LWP) data from ground-based microwave radiometry, so this break in the scaling

of Landsat radiances may be influenced by saturation effects.

The transition to smoother behavior at scales of 0.2–0.4 km is the subject of this study; we will denote the characteristic transition scale η_{rad} and call it the "radiative smoothing scale." The best fit to Eq. (1) between 70 and 180 m (over 1000 k) yields $\beta \approx 3.4$, but we cannot rule out an exponential cutoff. The inset in Fig. 2 reproduces Cahalan and Snider's original energy spectrum showing the scale break. At the very smallest scales, we detect the presence of white ($\beta = 0$) digitization noise.

2) THE PHYSICAL-SPACE PICTURE

The robust feature at 0.2–0.4 km can be apprehended from another statistical vantage point, this time in physical space. Let $\varphi(\mathbf{x}) \in [0, 255]$ be the grayscale value, approximately proportional to nadir-viewing radiance, of the Landsat pixel at $\mathbf{x} = (x, y) \in [0, L - 1] \otimes [0, L - 1]$, where we adopt a unit of length where pixel size $\ell = 1$, hence outer-scale $L = 4096$. Following Monin and Yaglom (1975), we consider the "increment" $[\varphi(\mathbf{x} + \mathbf{r}) - \varphi(\mathbf{x})]$ over $\mathbf{r} = (r \cos \theta, r \sin \theta)$. Fields with $\beta < 1$ are stationary ("statistically" homogeneous) in the sense that their statistical properties are invariant under translation in $\mathbf{x}$. If $\beta > 1$, this statistical invariance is generally violated, the field being nonstationary per se; however, if $\beta < 3$, its increments are stationary. Spatial averages are only meaningful for stationary quantities.

In statistically isotropic situations, the "structure function" or "semivariogram" $\langle[\varphi(\mathbf{x} + \mathbf{r}) - \varphi(\mathbf{x})]^2\rangle$ is a function of $r = |\mathbf{r}|$ alone; this function $D_\varphi(r)$ is related to the energy spectrum by a Wiener–Khinchin theorem (e.g., Monin and Yaglom 1975):

$$D_\varphi(r) = 2 \int_0^\infty [1 - \cos 2\pi k r] E_\varphi(k) \, dk. \qquad (2)$$

The power law in Eq. (1) can be substituted into the above as long as $\beta \in (1, 3)$, yielding

$$D_\varphi = \langle[\varphi(\mathbf{x} + \mathbf{r}) - \varphi(\mathbf{x})]^2\rangle \sim r^{2H_2} \qquad (3)$$

with

$$H_2 = \frac{\beta - 1}{2} \in (0, 1). \qquad (4)$$

[The subscript 2 used here refers to the fact that we are considering only a second-order statistic, as opposed to $\langle|\varphi(\mathbf{x} + \mathbf{r}) - \varphi(\mathbf{x})|^q\rangle$ with any real q.] For instance, energy spectra in $k^{-5/3}$ are in Fourier duality with structure functions in $r^{2/3}$. If the field is stationary (i.e., $\beta < 1$, with some small-scale cutoff to avoid infinite variance), then Eq. (2) yields $D\varphi(r) = $ constant $+$ correction term in $1/r^{1-\beta}$, thus $H_2 = 0$ in Eq. (3). If the field is at least once differentiable ($\beta \geq 3$), then Eq. (3) leads in theory to $H_2 = 1$.
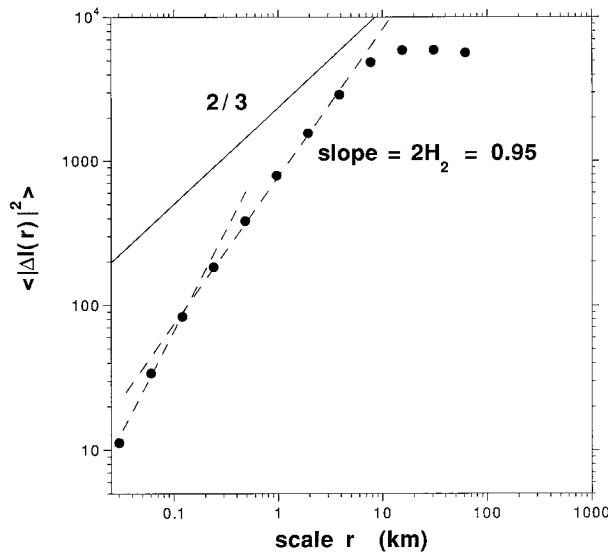
FIG. 3. Structure function for half the radiance field in Fig. 1. The same data as in Fig. 2; $D_I(r)$ was averaged over 2048 columns for 12 values of r, from $\ell = 30$ m to $L/2 = 2048\ell \approx 62$ km by factors of 2. A reference trend in $r^{2/3}$ corresponding to $E(k) \propto k^{-5/3}$ is indicated.

Equations (3) and (4) have a consequence that is important in the sequel: $\varphi(\mathbf{x} + \mathbf{r})$ and $\varphi(\mathbf{x})$ must generally be close if r is relatively small (cf. the appendix). In other words, large jumps between almost neighboring pixels are at best a rare occurrence. Following usage in the statistical literature, we will refer to this property as "stochastic continuity."

We have computed $D_\varphi(r)$ for $r/\ell = 1, 2, 4, \cdots, 2048 = (L/\ell)/2$, where $\ell = 30$ m using the same data as for Fig. 2 in the same manner, namely, analyzing the 2048 leftmost columns in Fig. 1, treating each one as a 1D field and averaging. The results are plotted versus r on log–log axes in Fig. 3, where the scale break is again apparent. The empirical value for the slope $2H_2 \approx 0.95$ is compatible with Eq. (4) for $\beta \approx 2.0$, given the typical uncertainties on such exponents (± 0.05). The transition to stationary behavior (slope ≈ 0) is observed at the integral scale. The transition to smooth behavior at η_{rad} is also seen; however, due to finite size effects and noise the small-scale slope assumes a spurious value smaller than 2 (which in theory corresponds to the differentiable case, $\beta \geq 3$ and $H_2 = 1$).

b. Explanations

1) PHYSICAL THEORIES

Cahalan and Snider (1989) noted that the smoothing scale is close to the nominal geometrical thickness $\Delta_z \approx 200$–400 m for marine Sc, recalling that Δ_z is more or less the size we expect for a convection cell. Furthermore, it is conceivable that the prevailing turbulent dynamics unfold in 3D below this scale and in 2D above this scale where, according to Kraichnan's (1967) phe-

nomenology, an inverse (small-to-large eddy) enstrophy cascade predicts a $k^{-5/3}$ spectrum. However, we have shown elsewhere (Davis et al. 1994, 1996a) that in situ probings of LWC fluctuations in marine Sc are scale invariant from a few tens of meters to a few tens of kilometers; no special behavior occurs at cloud-thickness scale nor at that of the whole boundary layer. This makes a dynamical mechanism that controls internal cloud structure an unlikely explanation for the Landsat scale break.

Cahalan and Snider also point to a possible connection between η_{rad} and the mean free path (MFP), $\langle\sigma\rangle^{-1}$, where $\langle\sigma\rangle \approx 40$ km^{-1} is the mean value for extinction. This quantity is estimated empirically from the mean optical thickness $\langle\tau\rangle = \langle\sigma\rangle\Delta_z \approx 13$, as obtained from their passive microwave radiometry. To correct for the effects of forward scattering, we can use the "transport" MFP: $l_t = [(1 - g)\langle\sigma\rangle]^{-1} \approx 150$ m $\approx 0.5\Delta_z$, where $g \approx 0.85$ is the usual asymmetry factor value for cloud droplet phase functions. If we use the most probable value of τ (≈ 6) instead of the mean, l_t would be about twice as large ($\approx\Delta_z$). The importance of l_t stems from the fact that we generally expect radiance to be insensitive to small fluctuations of extinction at scales much smaller than a transport MFP. This is because l_t is effectively the MFP for a single isotropic scattering, as opposed to $\approx(1 - g)^{-1}$ more or less forward ones. In other words, after traveling one transport MFP a photon has "forgotten" its original position and direction. Note that the transport MFP idea is relevant only if $\Delta_z/l_t = (1 - g)\langle\tau\rangle \gtrsim 1$, that is, one or more effectively isotropic scatterings occur for most photons. [Interestingly, our multiple scattering approach exposed in sections 3–5 shows that radiance indeed decorrelates from optical depth but at a somewhat larger scale, close to the harmopic mean of l_t and Δ_z, and this is readily explained within the diffusion approximation to radiative transfer.]

2) STATISTICAL THEORIES

Lovejoy et al. (1993) also sketch two explanations for the Landsat scale break that preserve the scaling of both cloud structure and the associated radiation fields. The authors first remark that the Landsat radiometer frequently saturates in cloudy scenes, the gray level is 255 (TM) or 127 (MSS) over large clusters of pixels and argue that this can cause a spurious scale break. In our Fig. 1, 17% of the pixels are indeed saturated and this ratio can reach as much as a third of all pixels, as in the rhs of Fig. 1. However, the data on the lhs used to obtain the statistics in Figs. 2 and 3 is only 7.6% saturated, and the numerical experimentation presented below shows that saturation affects the proportionality factor in Eq. (1), not the exponent nor the range of scales, at least within a large class of models with $\beta > 1$.

Second, Lovejoy et al. recall that scale invariance is only a statistical symmetry of the data and that every

realization (a single Landsat scene) can be nonscaling without preventing the whole ensemble (all possible scenes at that location, season, and time of day) from having perfect scaling. In other words, we are suffering from insufficient sampling. The authors further argue that Welch et al.'s (1988) power law area/perimeter relations do not break at the observed range of values for η_{rad}, namely, 0.1–0.5 km (H. Barker and S. Gollmer, personal communications). However, area/perimeter analyses apply to broken cloud scenes, not to the almost completely overcast cases that are of interest here. Lovejoy's (1982) empirical relation is

$$\text{area} \sim \text{perimeter}^{4/3}, \tag{5}$$

in contrast to the Euclidian prediction, area $\sim$ perimeter^2. Marine Sc are very extended and thus fall at the end of the range of cloud sizes: *outer-scale* $\approx \sqrt{\text{area}} \approx 10^3$ km, perimeter $\approx 10^{4.5}$ km. Cahalan and Joseph (1989) investigated Lovejoy's law for different cloud types, finding that Sc follow a similar power law as long as the radiometric threshold used to define "cloud" is representative of cloud base. At any rate, areas and perimeters relate to the cloud's outer scale, and there is no conflict with the existence of a scale break in the internal structure and/or the associated radiation fields at much smaller scales.

3. Artificial Landsat data

In the appendix, we describe two kinds of scale-invariant random cloud models with $\beta > 1$ used in this study: bounded cascades (Cahalan et al. 1990, 1994a; Marshak et al. 1994) and fractionally integrated singular cascades (Schertzer and Lovejoy 1987; Wilson et al. 1991; Davis et al. 1996b). In particular, we discuss their "stochastic continuity," a two-point statistical property that plays a critical role for radiative transfer.

In this section, we describe then compare results for two methods of simulating radiance fields that in turn are analyzed in the same way as the Landsat data. One accounts for net horizontal fluxes excited by the variability, the other not. Only in the former case can we simulate the Landsat scale break in strictly scaling cloud models, thus demonstrating that a radiation transport mechanism mediated by horizontal fluxes is causing the scale break.

a. Independent pixel approximations

The simplest way of treating radiative transfer in a horizontally inhomogeneous cloud model, next to neglecting internal variability altogether, is to use an independent pixel approximation (IPA) (Cahalan 1989; Davis et al. 1993; Cahalan et al. 1994a). This amounts to applying plane-parallel theory on a per pixel basis. Using Monte Carlo results as a standard of comparison, Cahalan et al. (1994b) show that the IPA is very accurate for large-scale averages in the case of stratiform clouds
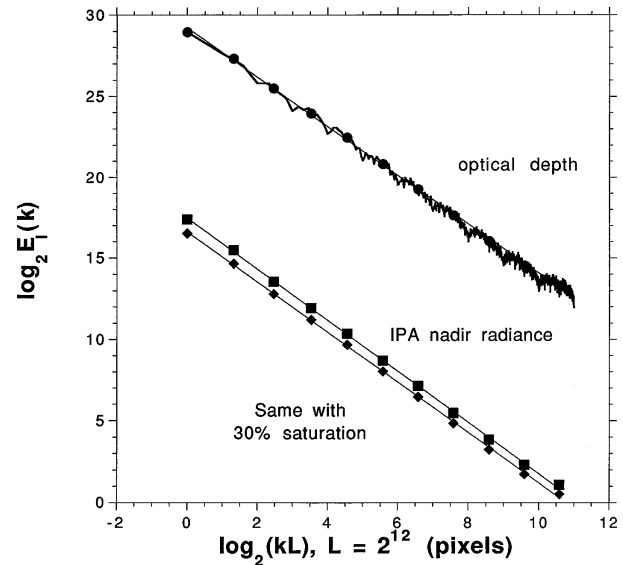

FIG. 4. Energy spectra of scale-invariant cloud models and IPA radiance fields. Optical depth fields $\tau(x)$ were similar to that in Fig. A2a (50 realizations were used). The IPA radiance field $I(x)$ was expressed as a bidirectional reflectance distribution function (BRDF): $\pi I(x)/\cos\theta_0$. The BRDF values were then digitized in Landsat radiometry fashion over 255 gray levels. The upper IPA case used a mapping of unit (or more) BRDF to 255, as if the instrument were designed to study highly reflective objects such as clouds. The lower curve corresponds to a 30% saturation at level 255, as in the worst situations reported for the actual Landsat images. All the spectra have almost the same scaling exponent $\beta \approx 1.5$.

with internal LWC fluctuations modeled with *bounded* cascades. Davis et al. (1993) find the opposite is true, but their cloud model is based on a *singular* cascade, which does not have the continuity property of its bounded counterparts.

We extend this work in two directions:

1) by computing radiances rather than albedoes;
2) by assessing the accuracy of the IPA in predicting the fluctuations of the radiation field, not only its average over the computational domain.

The first task is easily performed. Cahalan et al. (1994a) use an analytical expression for albedo that generalizes the two-stream result. Although there is no such expression for radiance, there are a number of Software packages that perform plane-parallel radiance computations; we used Stamnes et al.'s (1988) discrete ordinate code, DISORT. Since the only optical parameter that varies is $\tau(x)$, one can compute in advance enough radiances to generate a look-up table $I_{pp}(\tau)$ that covers the appropriate range in optical depth. We now compare the statistical properties of $\tau(x)$ and IPA radiance fields $I(x) = I_{pp}[\tau(x)]$.

Figure 4 shows three energy spectra in log–log axes. The top curve is for the $\tau(x)$ fields: 50 realizations of bounded cascades ($H = 1/3$, $p = 0.25$, 12 steps) with the mean $\langle\tau\rangle = 13$. At much smaller values than for

$E_\tau(k)$, we see two counterparts for the radiance field $I(x)$ obtained in the IPA for a Henyey–Greenstein (1941) phase function with $g = 0.85$ and sun angle $\theta_0 = 22.5°$ (as in Fig. 1). To better simulate Landsat measurements, radiance was represented as a bidirectional reflectance function and then digitized on 255 levels. The upper curve was obtained by mapping 255 to unity and mapping the digitized values back into [0, 1]. For the lower curve, 255 is mapped to all pixels equal or greater than some critical value; this value was chosen so that it produced a 30% saturation, a worst case scenario for Landsat cloud scenes. We see that the nonlinear mapping of τ to I, and subsequent digitization and (optional) truncation only changes the prefactor in Eq. (1), the scaling exponent β does not change significantly.

To see why this happens, we can use the physical space statistic $D_I(r)$, that is, the integral of $[I(x + r) - I(x)]^2$ weighted by the joint probability measure for $I(x + r)$ and $I(x)$. Because of the continuity property of the random field $\tau(x)$, the integrand can be approximated linearly by $[\tau(x + r) - \tau(x)]^2 |dI/d\tau|^2_{\tau = \tau(x + r/2)}$. The Jacobian $|dI/d\tau|$ being bounded, we have $D_I(r) \propto D_\tau(r)$ and proportionality for the energy spectra follows from Eq. (2). Furthermore, the above argument fails for higher-order structure functions $\langle [I(x + r) - I(x)]^q \rangle$, $q \gg 1$, if $\tau(x)$ is continuous but has a broad distribution of increments because of the effect of nonlinear terms in the expansion of $I[\tau(\cdot)]$ around $x + r/2$; this indeed occurs for multifractal $\tau(x)$ fields (Marshak et al. 1995).

In summary, the IPA, a nonlinear but monotonic mapping from τ to radiance, predicts accurately (in the sense of low-order statistics) the fluctuating radiance field in regimes where it is valid, task (2) in the above. In the following, we address this question of IPA validity by comparing its results with those of a numerically exact approach to radiation transport in variable media, namely, Monte Carlo.

b. Monte Carlo methodology

A better but more costly way of computing a radiance field than IPA is to run a Monte Carlo (MC) simulation. For flux computations, MC is algorithmically simple, using only the most basic elements of kinetic theory. Straightforward MC is competitive with any other general solution of numerical radiative transfer problems for domain-average quantities but requires large amounts of computer time to reduce the idiosyncratic noise at the pixel scale. Furthermore, for accurate radiance computations, we rely on a variance-reduction technique based on "local estimation" (see Marchuk et al. 1980 or Marshak et al. 1995 for details).

The stochastic continuity of the extinction field is as important here as in the IPA. Given the local value of extinction $\sigma(x)$, one can define a local MFP. However, photons propagating in heterogeneous media have different free path distributions, hence means, between scatterings at different points and in different directions.

Moreover, it can be shown on general grounds that, on average, geometrical free path distributions are no longer exponential (Davis 1992); consequently, a single MFP value (e.g., the "mean" MFP) can no longer define it completely. If the medium is continuous, however, then the photon encounters rather small changes in extinction as it cumulates path. If, moreover, pixels are, on average, optically thick in the horizontal, then few pixel boundaries are crossed between two scattering events. In these circumstances, a mean-field approach (i.e., one that assumes there is a uniform/isotropic value of the MFP) should work relatively well. Diffusion theory is precisely such an approach, and we use it later on to model statistically MC photon trajectories and, from there, to explain the Landsat scale break.

c. IPA and MC fields compared

1) VISUAL COMPARISON

Figure 5a shows IPA and MC nadir radiance fields for the same one-dimensional cloud model as in Fig. A1 with, however, 10 cascade steps rather than 12. This is consistent with Cahalan and Snider's (1989) analyses of FIRE data (leading to $\langle \tau \rangle \approx 13$, $\beta \approx 5/3$, $p \approx 0.25$) and Davis et al.'s (1994, 1996a) observation of three decades of scaling. The geometrical and optical parameters reflect the general conditions during FIRE ($\Delta_z = 0.3$ km, $g = 0.85$) and for the Landsat scene in Fig. 1 in particular ($\theta_0 = 22.5°$). For the 2×10^8 photon MC simulation, the pixel size ℓ is set to 12.5 m, somewhat less than the 30-m Landsat resolution and close to the inner scale in Davis et al.'s (1996a) LWC data. The outer scale is therefore $L = 2^{10}\ell \approx 12.8$ km, not far from their (admittedly uncertain) estimate of the integral scale for LWC fluctuations, ≈ 20 km; horizontally cyclical boundary conditions are used beyond this scale.

The more realistic MC field is visibly smoother than the IPA prediction. Figure 5b shows a zoom onto a 1-km portion of Fig. 5a, highlighting the empirical uncertainties ($\approx 1\%$ on average) on the nadir radiances obtained by local estimation. We now quantify and parameterize the smoothing that occurs as soon as we relax the IP assumption, thus allowing for horizontal fluxes.

2) STATISTICAL COMPARISON

Figure 6 is a log–log plot of $E_I(k)$ for MC nadir radiances. Continuing to emulate the Landsat observations, the radiance field was first saturated at the 8% level then digitized over a 255 grayscale. Two realizations of the cascade were used and their spectra were averaged. In spite of this averaging, the statistical noise remains strong and it is helpful to represent $E_I(k)$ using octavewide wavenumber bins (Davis et al. 1996a). We note the inevitable presence of numerical MC noise at the very smallest scales.

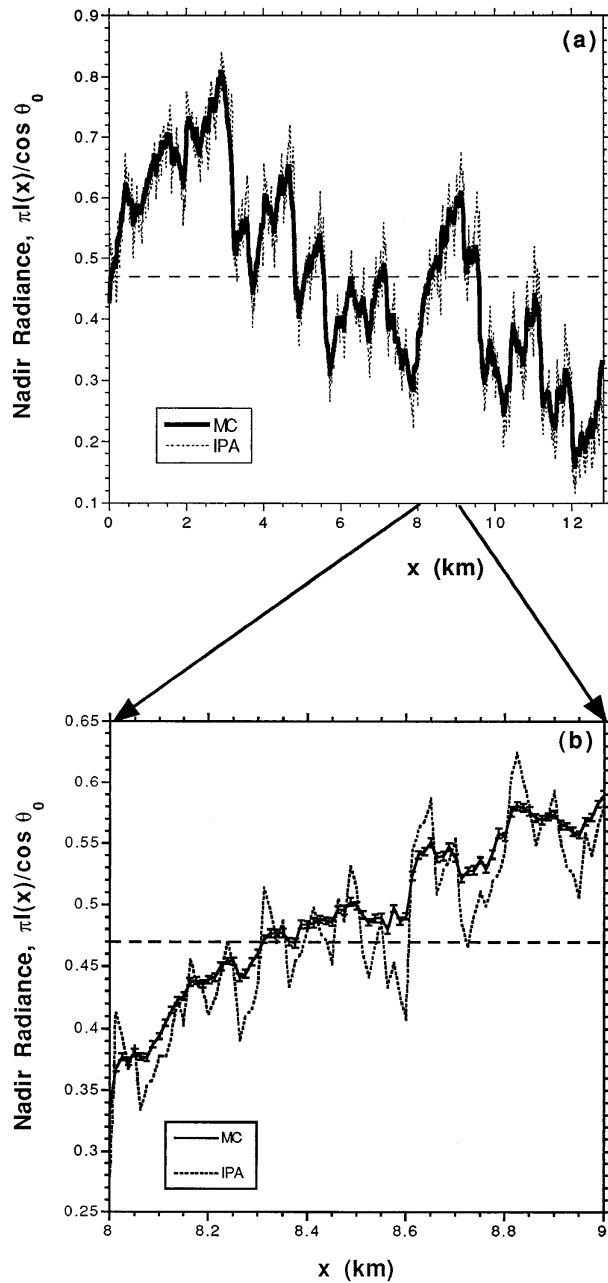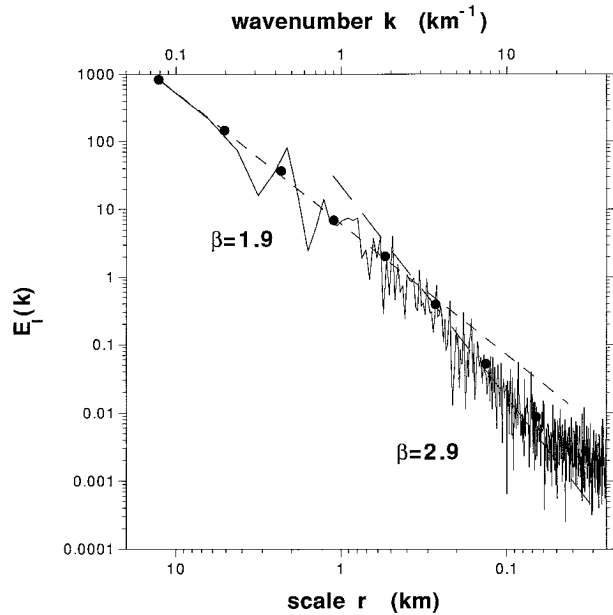The large-scale spectral slope in Fig. 6 is ≈ 2 as in

Fig. 6. Energy spectrum of MC radiance fields. The MC field in Fig. 5a was saturated at 8% and digitized on 255 levels, emulating closely the way Landsat data is captured, and another realization was added. The scale break occurs at $\approx$400 m, and white MC noise is apparent at the smallest scales.

Fig. 2 and the scale break occurs around 400 m, about twice the value of η_{rad} in Fig. 2. This is a deliberate choice, forced by the current limits of our computational power. Indeed, Fig. 2 uses the equivalent of 2048 realizations of a 12-step cascade and radiance is measured to within $\approx$1:255 accuracy. As a result of our parameter choices, the mean and variance are somewhat larger in Fig. 5a than in Fig. 1. In the following, we show how η_{rad} depends on cloud parameters.

Figure 7 is the theoretical counterpart of Fig. 3: it shows the structure functions $D_I(r)$ for both the MC and IPA fields. The break at $\eta_{rad} \approx 400$ m is clear and we see that the IPA works fairly well for scales larger than η_{rad}. For a more systematic comparison of MC and IPA fields beyond spectral (second order) statistics, we refer to Marshak et al. (1995) who use multifractal techniques to quantify the breakdown of the IPA at large scales with higher-order statistics.

d. Factors controlling the smoothing scale

It is of interest to explore the dependence of η_{rad} on the optical ($\langle\tau\rangle$ and g) and geometrical (θ_0, Δ_z, L, and ℓ) parameters of the problem, as well as their structural counterparts (H, p, and/or choice of variability model). In Table 1 we summarize the parameter ranges we used.

As for cloud models, both fractionally integrated and bounded cascades gave similar results as long as a relative measure of their variance, such as $\sigma_\tau/\langle\tau\rangle$ and the spectral exponent β, remains constant. Increasing β (min$\{2H, 1\}$ + 1 for bounded models) and decreasing

Fig. 5. Comparison of IPA and MC nadir radiance fields. The optical depth field in Fig. A2a was used with 10, rather than 12, cascade steps. (a) The whole computational domain of size L =12.8 km is plotted; the thickness of the MC line is roughly the uncertainty. (b) A 1-km zoom into panel (a) showing the $\approx$1% empirical error bars on the pixel scale (ℓ = 12.5 m) radiances that were obtained by local estimation (see text). The cloud's thickness Δ_z was set to 300 m and it was irradiated with 200 $\times$ 10^6 photons coming in at θ_0 = 22.5°; scattering was determined by a Henyey–Greenstein phase function with g = 0.85; periodic boundary conditions were applied in the horizontal.
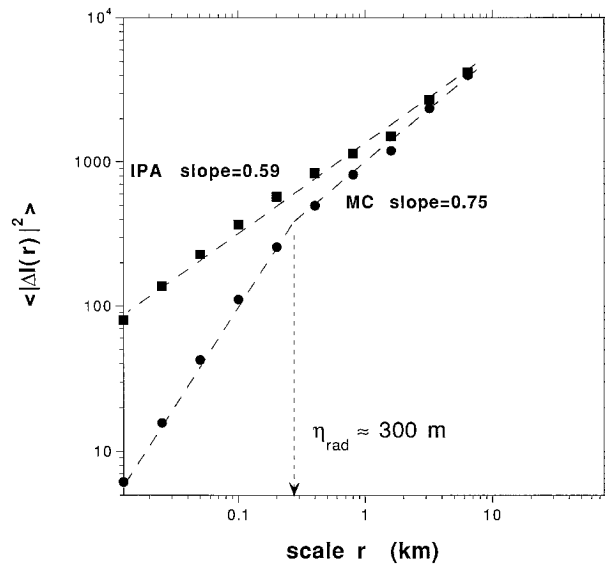
FIG. 7. Structure functions of IPA and MC radiance fields. The same data as in Figs. 5 and 6 were used. Note the scale break and the approximate agreement of the two methods at large scales.

σ_τ (with $p \to 1/2$ for bounded models) both lead to smaller variability at all scales and smaller η_{rad} values. Varying L and ℓ has no effect on η_{rad} as long as they straddle this scale with enough distance to operationally define the two distinct regimes; in particular, the latter is kept as far below η_{rad} as possible to avoid contamination by MC noise of scales near the break. We also found η_{rad} to be insensitive to θ_0, excluding grazing angles where the radiance field becomes highly variable at all scales and decoupled from the optical depth field due to strong shadowing (rather than smoothing) effects.

Figure 8 illustrates the dependence of η_{rad} on the remaining parameters: $\langle\tau\rangle$, g, and Δ_z, for 12-step bounded cascade models (two realizations) with $H = 1/3$, $p = 0.25$, and $\theta_0 = 0°$. Using $D_I(r)$, Fig. 8a shows that η_{rad} is reduced by a factor of ≈ 2 when $\langle\tau\rangle$ quadruples, Fig. 8b that going from $g = 0$ to $g = 0.85$ increases η_{rad} by a factor of ≈ 3, and panel Fig. 8c that doubling Δ_z roughly doubles η_{rad}. These dependencies are now explained

in the framework of a mean-field Green function approach.

4. Green function analysis of horizontal photon transport

Radiative smoothing is clearly a consequence of horizontal photon transport driven by the gradients in the optical depth field. To explain the dependence of η_{rad} on $\langle\tau\rangle$, g, and Δ_z, we adopt a naive method of quantifying horizontal transport. A large number of photons are injected into a model cloud from a single point on the upper boundary, and we observe where they ultimately escape from the cloud. From a theoretical perspective, we generate a radiance distribution at all points of space from a δ-function source term in the radiative transfer (or linear transport) equation. The resulting radiance field is called interchangeably "Green function," "impulse response," or "point-spread function" of the optical medium. From an instrumental perspective, we are irradiating the cloud with an ideal laser beam—an idea we pursue in section 6.

We will restrict our focus to the remotely observable part of this radiative response, that is, photons escaping the cloud from various boundary points in various directions. With this caveat, we will designate this limited sample of the whole radiance field as a Green function.

a. "Spots" of reflected and transmitted light associated with a point source

Photons start their trajectories in a plane-parallel medium at a horizontal position $(x_{in}, y_{in})^T$ on the upper boundary ($z_{in} = 0$) and the illumination pattern is kept azimuthally symmetric (i.e., a collimated beam normal to the boundary or a diffuse point source). We are interested in the statistics of the photon's cumulative horizontal displacement vector,

$$\boldsymbol{\rho} = \begin{pmatrix} x_{out} - x_{in} \\ y_{out} - y_{in} \end{pmatrix}, \quad (6)$$

especially it's Euclidian norm,

TABLE 1. Exhaustive list of cloud model parameters with values used in this study; those that have a first-order effect on horizontal transport are italicized.

| Cloud model parameter	Symbol	Typical value	Range
Mean optical thickness	τ, $\langle\tau\rangle$	13	2–64
Variance parameter	$\sigma_\tau/\langle\tau\rangle$	0.5	0–0.7
Geometrical thickness	Δ_z	300 m	200 m–400 m
Grid size	L	12.8 km	6 km–20 km
Grid constant	ℓ	12.5 m	6 m–60 m
Number of pixels	(L/ℓ) in 1D	1024	1024–4096
	$(L/\ell)^2$ in 2D	$128^2 = 16,384$	
Wavenumber spectrum	$E(k)$, $k \geq 0$	$\propto \delta(k)$, homogeneous	
	$0 < k \leq 1/(2\ell)$	$\propto k^{-(2H+1)}$, fractal	$H = \frac{1}{3}$
Asymmetry factor	g	0.843	0–0.85
Solar angle	θ_0	22°	0°–60°
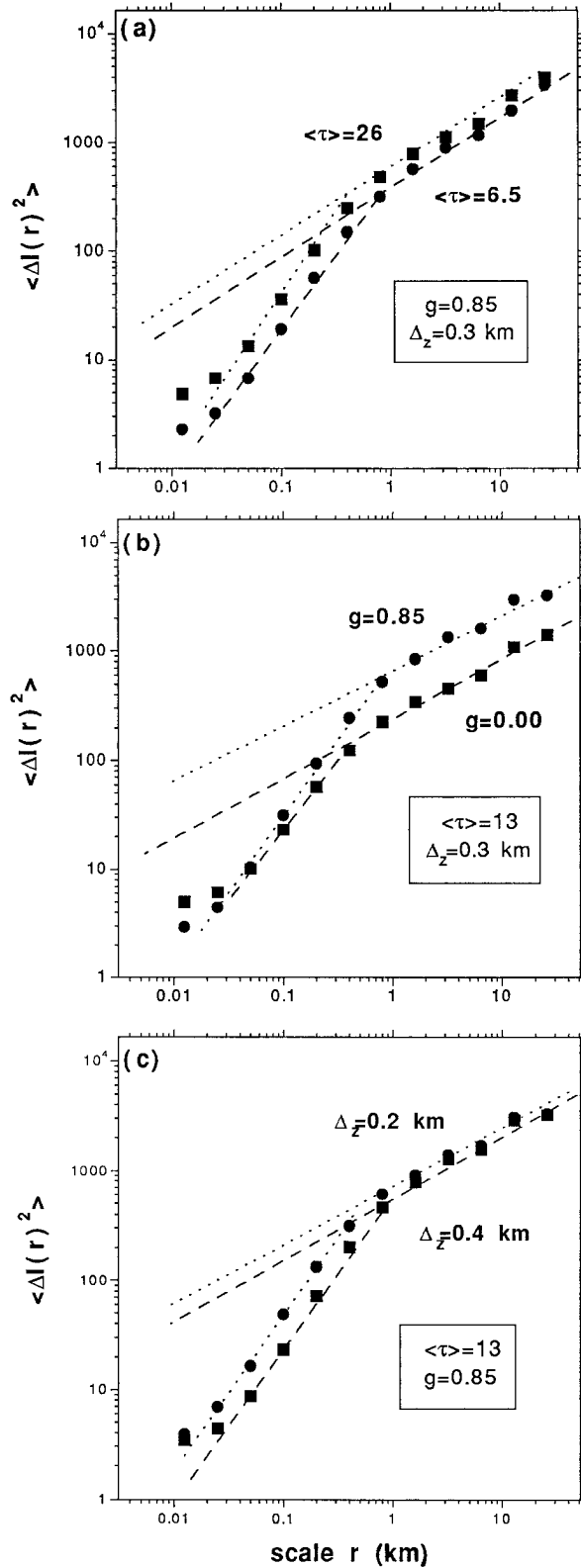
FIG. 8. Structure functions for MC radiance fields. The effects on η_{rad} of (a) multiplying $\langle\tau\rangle$ by 4, (b) going from $g = 0$ to $g = 0.85$, and (c) doubling Δ_z are illustrated.

$$\rho = \sqrt{(x_{out} - x_{in})^2 + (y_{out} - y_{in})^2}, \quad (7)$$

for reflectance ($z_{out} = 0$) or transmittance ($z_{out} = \Delta_z$). In the former case, the 2D probability density function (PDF) of $\boldsymbol{\rho}$ can be obtained either from the albedo field $R(x, y)$ for escape in any direction, or from its radiance counterpart $I(x, y)$ for escape in direction of the zenith (i.e., nadir-viewing radiance). We are primarily interested in low-order moments: $\langle\rho\rangle$ and $\langle\rho^2\rangle$. The cloud model can be homogeneous, $\tau(x, y) \equiv \langle\tau\rangle$, or randomly variable in either one or both horizontal directions, using scale-invariant models. If the variability is 1D, $\tau(x)$ is piece-wise constant over a domain $0 \leq x < L$ on a grid of pixel size $\ell \ll L$ and considered periodic outside of $[0, L)$ with period L, similarly in 2D.

Composite Fig. 9 shows logarithmically spaced isophotes for the 2D albedo and transmittance fields obtained from two normally illuminated cloud models, fractal or not, with geometrical thickness $\Delta_z = 300$ m, optical thickness $\langle\tau\rangle = 13$, and Henyey–Greenstein scattering with $g = 0.85$. In the homogeneous case, responses are described by a series of concentric circles that, as the distance to the beam increases, become equidistant; this implies an exponential decay. Responses for the fractal case show a degree of anisotropy traceable to the variability in $\tau(x, y)$; also the root-mean-square (rms) displacements $\sqrt{\langle\rho^2\rangle}$ are larger here than in the homogeneous case.

b. Scaling properties of $\langle\rho\rangle^2$

We have plotted $\langle\rho^2\rangle/\Delta_z^2$ as a function of $(1 - g)\langle\tau\rangle$ for homogeneous and fractal models in Figs. 10a,b respectively; results pertaining to albedo, nadir radiance, and transmittance are shown. A total of 24 simulations were used: $\langle\tau\rangle = 2, 4, 8, 16, 32, 64$, for $g = 0$ and $g = 0.85$, in both cases. We see

1) good "collapse" of the results for albedo and transmittance, with

$$\langle\rho^2\rangle \approx \Delta_z^2 \begin{cases} [(1 - g)\langle\tau\rangle]^{-1} & \text{for albedo} \\ \text{constant} & \text{for transmittance} \end{cases} \quad (8)$$

2) cloud-top $\langle\rho^2\rangle$'s slightly larger for fractal models than for homogeneous ones at given $\langle\tau\rangle$
3) radiance-based $\langle\rho^2\rangle$'s slightly larger than their albedo-based counterparts (and not quite as good collapse).

This small discrepancy between radiance- and albedo-based $\langle\rho^2\rangle$ reflects that flux is an integral over radiance and, in this particular problem, the radiance is not expected to be isotropic: at a given point, there will be many more photons coming from the general direction of the localized source because of the exponential decay with ρ. In other words, using albedo as a standard for comparison, radiance in the zenith direction is not representative of this particular value of ρ but of a somewhat larger one.
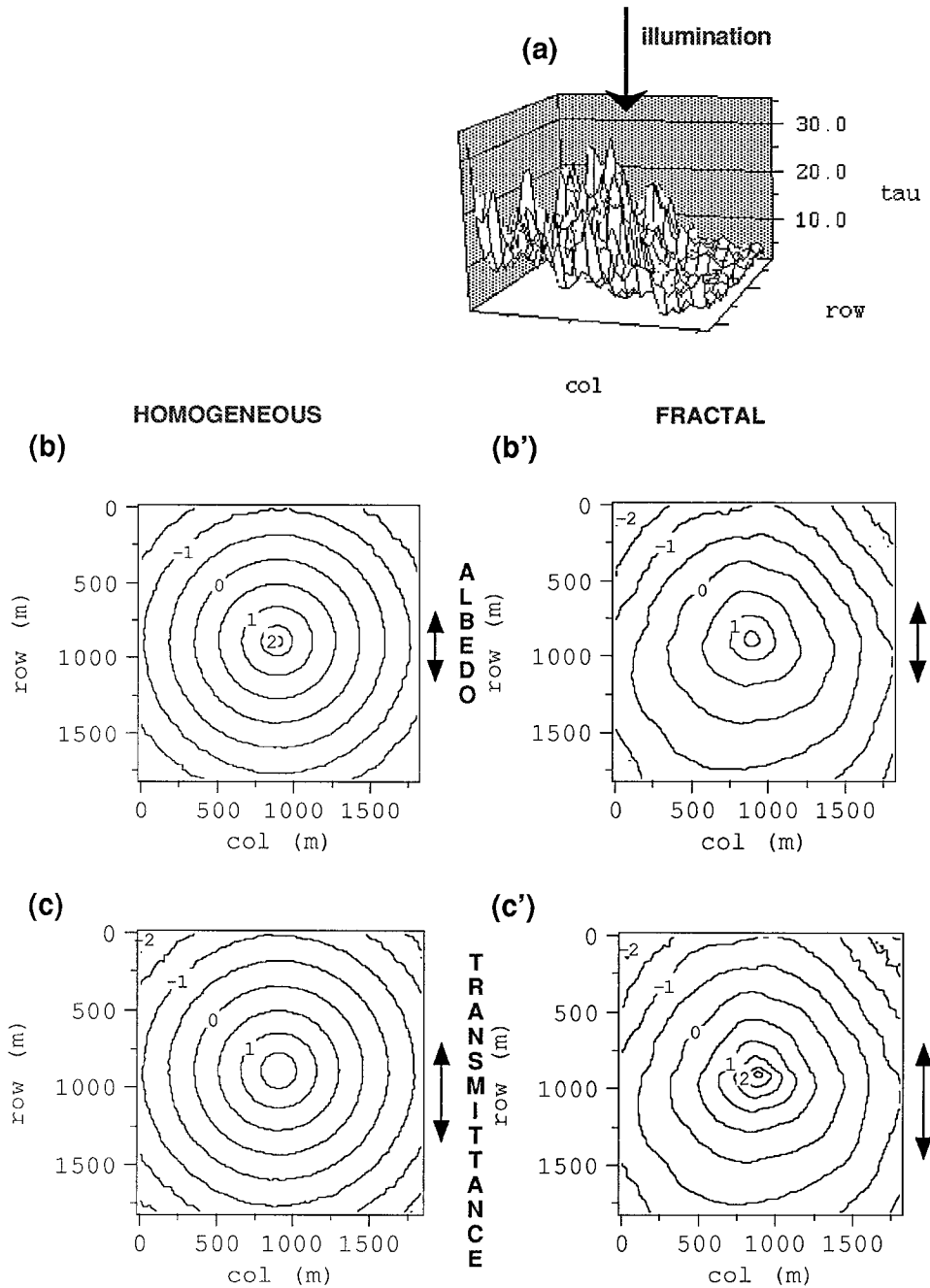
FIG. 9. Spots for artificial 2D homogeneous and fractal clouds with anisotropic scattering. (a) Central 2 km × 2 km portion (60 pixel × 60 pixels) of a cloud model based on a 2D bounded cascade model (Davis et al. 1996c) with $\langle \tau \rangle = 13$ on a 128 × 128 grid ($L = 2^7\ell \approx 4.3$ km). In these MC simulations with 10^8 histories, the phase function was Henyey–Greenstein with $g = 0.85$ and the illumination from zenith. (Note the roughening effect of MC noise in the corners where the lowest light levels occur; typical errors go from $\approx 0.5\%$ in the center to $\approx 5\%$.) (b) Reflected spot, using flux (local albedo), for a homogeneous cloud with $\tau = 13$. (b') Same as (b) for the fractal model in panel (a), overall transmittance $T \approx 0.5$. (c, c') Same as (b, b') for spots in transmittance. Isophotes are traced for integer values on a $\log_{10}$ scale; the flux units are arbitrary but uniform, so the higher values and slower spread in panel (c') compared to (c) lead to a substantially larger overall transmittance $T' \approx 0.7$. The rms horizontal displacement $\sqrt{\langle \rho^2 \rangle}$ is shown for each plot.
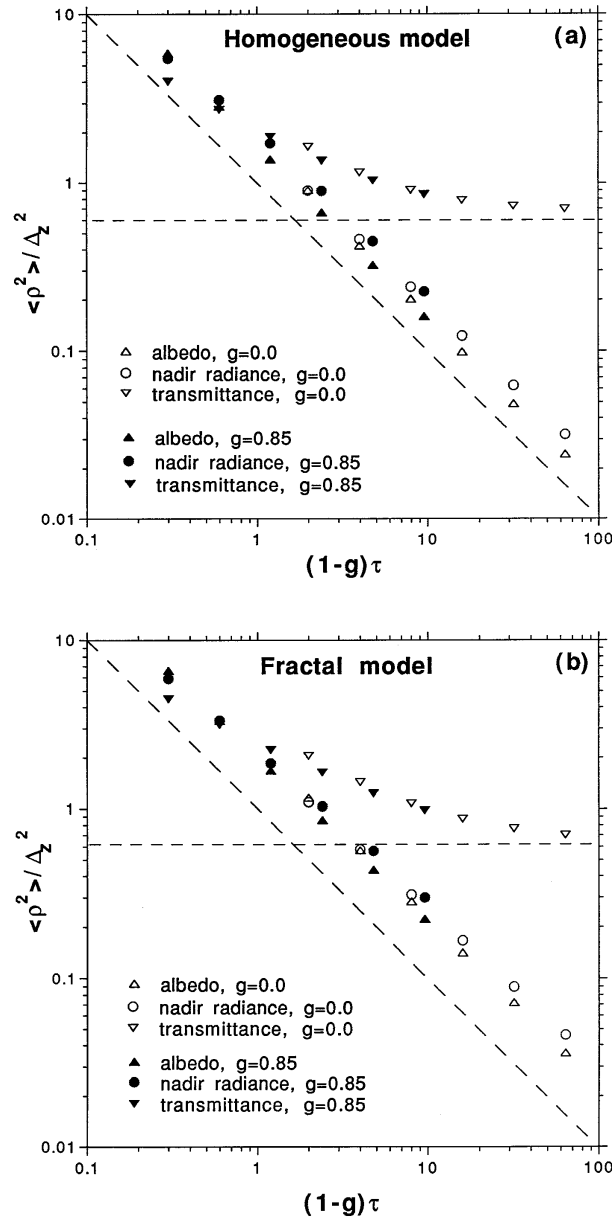
FIG. 10. Scaling properties of $\langle \rho^2 \rangle$ for (a) homogeneous and (b) fractal clouds. Transmittance, albedo, and nadir radiance are represented. The fractal variability was generated using the bounded cascade in Fig. A2a but with different multipliers.

Finding 2) is a direct consequence of Jensen's (1906) inequality. To estimate $\langle \rho^2 \rangle / \Delta_z^2$ for the fractal model, we compute, in the spirit of an IPA, the average of $[(1 - g)\tau]^{-1}$ over the appropriate PDF for τ. This will yield more than the "mean field" result $[(1 - g)\langle \tau \rangle]^{-1}$ simply because of the convexity of the function τ^{-1}.

The first and most important numerical result is now explained physically by photon diffusion processes, summarizing Davis et al.'s (1996c) derivation from first principles.
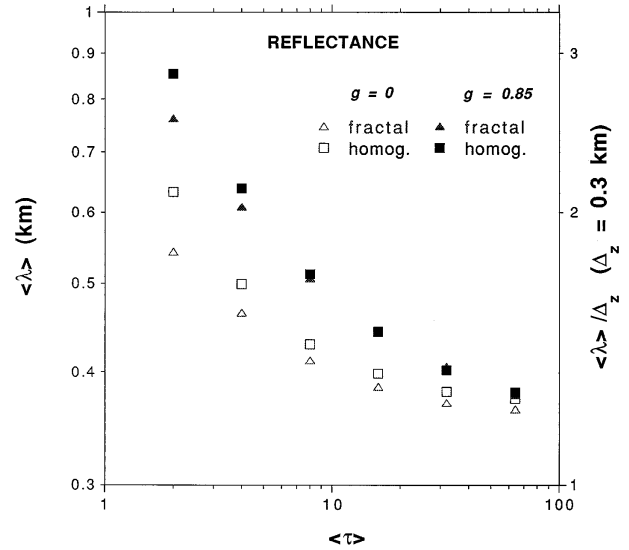

FIG. 11. Mean total path $\langle \lambda \rangle$ of reflected photons for homogeneous and fractal clouds. We see that $\langle \lambda \rangle = \langle ct_R \rangle \sim \Delta_z \times \{1 + correction[(1 - g)\tau]\}$ for the same cloud models as in Fig. 10.

c. Diffusion theory for $\langle \rho^2 \rangle$

The results in Eq. (8) follow naturally from Davis and Marshak's (1996) exact analytical solution of the Green function problem in the diffusion approximation. This implies that the MC trajectories can be modeled in this context as random walks. Following Davis et al. (1996c), we make the heuristic assumption that, while in the cloud, photons are in Brownian motion (BM). Total displacement $\mathbf{r}(t)$ at time t will then obey

$$\langle \mathbf{r}^2(t) \rangle = \langle \rho(t)^2 \rangle + \langle z(t)^2 \rangle = Dt, \qquad (9)$$

where diffusivity D is the velocity of light c times the "transport" mean free path l_t (Case and Zweifel 1967). The usual cloud parameters give

$$D = \frac{c\Delta_z/\tau}{1 - g}. \qquad (10)$$

The nontrivial result from BM theory used by the authors is that the mean time for a photon to escape the cloud from above is

$$\langle t_R \rangle \sim \frac{\Delta_z}{c}, \qquad (11)$$

independently of D (hence τ and g). As justification for Eq. (11), Fig. 11 shows total in-cloud path $\langle \lambda \rangle = \langle ct_R \rangle$ obtained by MC; there is little difference between fractal and homogeneous clouds here due to the insensitivity of $\langle t_R \rangle$ to the variable quantity, namely, τ. For a survey of the radiative transfer literature pertaining to the result in Eq. (11), we refer to Marshak et al. (1995).

Since $z(t) \equiv 0$ upon reflectance, we obtain $\langle \rho(t_R)^2 \rangle \approx \langle \rho(\langle t_R \rangle)^2 \rangle = D\langle t_R \rangle \sim \Delta_z^2/[(1 - g)\tau]$ from Eqs. (9)–(11). The result for spot size in transmittance follows from geometry: a "wave" of diffusing photons is emanating

from a point on the upper boundary and propagating slowly but isotropically, therefore $\langle \rho^2 \rangle = (2/3)\langle z^2 \rangle = (2/3)\Delta_z^2$ at cloud bottom, irrespective of g and τ.

For future considerations, it is important to note that the PDF of t_R is quite broad. To see why, we recall that average radiance (photon density) in a nonabsorbing scattering medium decreases only linearly with depth; so it is not so rare that photons penetrate the cloud deeply before eventually being reflected, rather than transmitted. In contrast with the mean prediction in Eq. (11), the return time for these highly scattered photons is about twice the characteristic time for transmittance; namely,

$$\langle t_T \rangle \sim \frac{\Delta_z^2}{D} = \frac{(1-g)\tau\Delta_z}{c} \sim (1-g)\tau\langle t_R \rangle. \quad (12)$$

5. Connection between the reflected Green function and the smoothing scale

a. Parameteric representation of Green functions with Gamma distributions

Figure 12 shows two PDFs for ρ associated with the same homogeneous and fractal clouds as described in the previous section except that in the latter case the variability is now 1D, allowing more cascade steps; furthermore, diffuse illumination conditions are applied. These PDFs are related to the axisymmetric radiance field by $dP/d\rho \propto \rho I(\rho)$. For the fractal model, the photons are injected at random in $(0, L)$ to obtain $\langle I(\rho) \rangle$, the symmetric spatially averaged Green function. The semi-log axes emphasize the exponential decay in the far field.

Davis and Marshak (1996) obtain closed-form expressions for the Fourier-cosine transforms of $R(\rho)$ and $T(\rho)$ in the framework of homogeneous diffusion theory in 2D. We note here the excellent approximation for all values of ρ by a Gamma distribution:

$$\frac{dP}{d\rho} = \rho I(\rho) \bigg/ \int_0^\infty \rho I(\rho)\, d\rho$$

$$\approx \frac{\alpha^\alpha}{\Gamma(\alpha)} \left[\frac{\rho}{\langle\rho\rangle} \right]^{\alpha-1} \exp[-\alpha\rho/\langle\rho\rangle]/\langle\rho\rangle. \quad (13a)$$

This well-known PDF has only two parameters, $\langle\rho\rangle$ and

$$\alpha = \frac{\langle\rho\rangle^2}{\text{var}[\rho]} = \left[\frac{\langle\rho^2\rangle}{\langle\rho\rangle^2} - 1 \right]^{-1}. \quad (13b)$$

The radiance data in Fig. 12 for the homogeneous and fractal cases yields $\langle\rho\rangle \approx 215$ and 224 m, $\alpha \approx 1.37$ and 1.16, respectively; similar fits were obtained for albedo and transmittance by Marshak et al. (1995). Note that, when $\alpha < 2$, the Green function itself, $I(\rho) \propto (dP/d\rho)/\rho$, is highly concentrated at the origin (largely due to the numerous low-order scatterings).
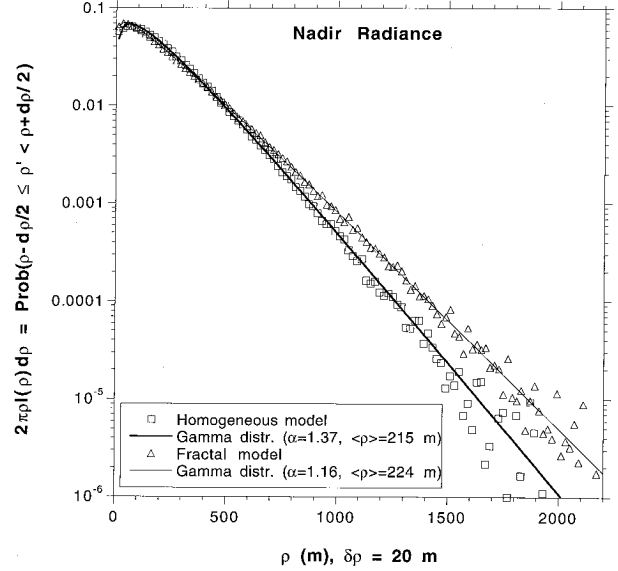

FIG. 12. PDF for nadir-viewing radiance as a function of ρ from a diffuse point source. This is a convenient representation of our MC estimates the Green function ("spot shape") in radiance: $I(\rho) = \text{PDF}/(2\pi\rho)$ increases very sharply at $\rho = 0$. We used homogeneous and fractal cloud models with $\langle\tau\rangle = 13$, $g = 0.85$ (Henyey–Greenstein phase function), and $\Delta_z = 300$ m. In the fractal case, the variability was simulated with a 10-step bounded cascade in 1D with $H = 1/3$ and $p = 0.25$, pixel size $\ell = 6.25$ m (hence $L = 2^{10}\ell \approx 6.4$ km); furthermore, the photons were injected at random points, meaning that $I(\rho)$ represents in this case a spatially averaged Green function $\langle I(\rho) \rangle$. Approximate PDFs using Gamma distributions with $\alpha < 2$, as obtained from Eqs. (13a,b), are also plotted.

b. Going from $\sqrt{\langle\rho^2\rangle}$ to η_{rad}

Our results in Fig. 8 for η_{rad}, based on the correlation statistics of the radiance fields associated with scale-invariance cloud models, have the same scaling properties as the rms horizontal transport $\sqrt{\langle\rho^2\rangle}$ for albedo or nadir radiance. This means that the scale break is traced to horizontal photon transport.

A closer examination tells us the proportionality factor between η_{rad} and $\sqrt{\langle\rho^2\rangle}$ or $\langle\rho\rangle$. The same fractal cloud model that yields the radiance field used to obtain Fig. 8b, with $\eta_{rad} \approx 0.6$–1.0 km, is used to obtain the (Green function related) data in Fig. 12, for which we have $\langle\rho\rangle \approx 0.2$ km, $\sqrt{\langle\rho^2\rangle} \approx 0.3$ km and hence $\alpha \approx 1.16$ from Eq. (13b). We now recall that the Gamma distribution reverts to an exponential one for $\alpha = 1$. For the exponential distribution, $\sigma_\rho = \sqrt{\langle\rho^2\rangle - \langle\rho\rangle^2} = \langle\rho\rangle$, hence $\sqrt{\langle\rho^2\rangle} \approx \sqrt{2}\langle\rho\rangle$ if $\alpha \approx 1$. The "3σ" rule (of Gaussian fame) can be adapted to this situation:

$$\text{Prob}\{\rho \geq 3\sigma = 3\langle\rho\rangle\} = e^{-3} \approx 0.05, \quad (14)$$

meaning that $\approx$95% of the reflected photons escape at less than $\approx 3\langle\rho\rangle$'s away from their entry point if $\alpha \approx 1$. Some photons travel farther and backtrack before escaping; these carry information about cloud density beyond the 3σ mark and cause further radiative smooth-

ing. In summary, we can say that $\eta_{\mathrm{rad}}/\langle\rho\rangle \approx 3\text{–}4$, equivalently,

$$\frac{\eta_{\mathrm{rad}}}{\sqrt{\langle\rho^2\rangle}} \approx 2\text{–}3. \qquad (15)$$

This is consistent with our findings in Figs. 8b and 12.

At present we have no quantitative way of empirically validating the result in Eq. (8) for the scaling of the Green function in transmittance, telling us that the size of the transmitted spot is commensurate with cloud thickness, independently of its density ($\langle\tau\rangle$) and scattering properties (g). This means that, for $\langle\tau\rangle$ large enough for photon diffusion to prevail, an inhomogeneous cloud will appear to be smoother from below than from above, as is commonly observed for Sc. (Of course, there can be even stronger reasons for this in real clouds, in particular, the fact their inhomogeneity increases with altitude.)

6. Implications for cloud remote sensing at visible wavelengths

The success of diffusion theory in predicting $\langle\rho^2\rangle$ and η_{rad} can be justified after the fact by King et al.'s (1990) utilization of in situ radiometry along 1D transects through marine Sc to locate extensive "diffusion domains." These are regions where radiance sampled in an azimuthal plane is approximately cosine in zenith angle. Although diffusion theory is known to break down at cloud boundaries, it seems to dominate the bulk of the radiation flow in Sc and can therefore be applied to a variety of cloud remote sensing techniques.

a. Passive methods

1) OPTIMAL SCALES AND METHODS FOR OPTICAL DEPTH RETRIEVAL

An immediate consequence of the radiative smoothing phenomenon is that, below the scale $\sqrt{\langle\rho^2\rangle}$ (or even η_{rad}), a remote observer is completely blind to the cloud's internal variability and his operational IPA breaks down.

This breakdown is now illustrated from the standpoint of optical depth retrieval. First, a look-up table of τ as a function of nadir radiance I_{pp} for a homogeneous plane-parallel cloud is compiled using DISORT with the appropriate phase function and solar angle (i.e., a Henyey–Greenstein model with $g = 0.85$ and $\theta_0 = 22.5°$); this relationship $\tau_{\mathrm{pp}}(I)$ is shown in Fig. 13a. Monte Carlo radiances for every pixel at some scale $r \in [\ell, L]$ are fed into this simple retrieval scheme and the outcome $\tau_{\mathrm{ipa}}(r; x)$ is compared with the known value

$$\tau_{\mathrm{true}}(r; x) = \frac{1}{r} \int_{x}^{x+r} \tau(x')\,dx'. \qquad (16)$$

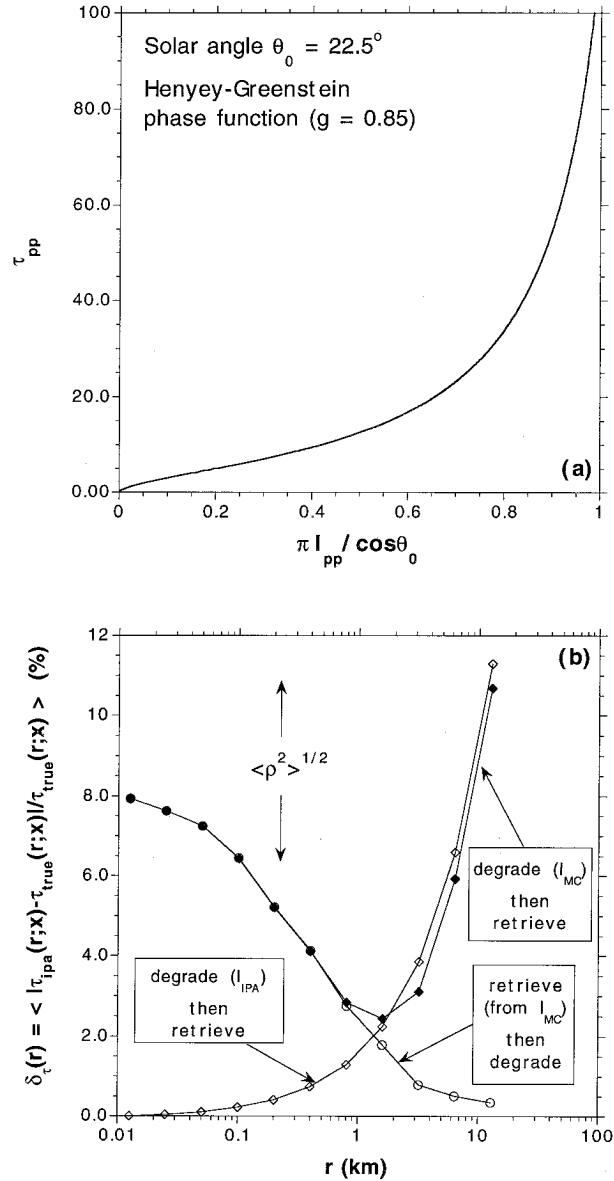The relative retrieval error is then averaged over non-overlapping r-sized pixels and realizations, yielding

FIG. 13. Average relative error in optical depth retrieval as a function of scale. (a) The plane-parallel optical depth–nadir radiance relation from DISORT used to retrieve optical depth from the same two realizations of the bounded cascade model used in Figs. 6 and 7. (b) Average retrieval $\delta_\tau(r)$ error vs scale r, averaging over position and realizations. The radiative smoothing scale $\sqrt{\langle\rho^2\rangle}$ indicates roughly the inflection point of the decreasing retrieve-then-degrade curve [Eq. (18b), open circles]. The degrade-then-retrieve curve [Eq. (18a), bold diamonds] bifurcates from this one because the convexity of the retrieval function in panel (a) plays an important role for scales larger than ≈ 1 km. This is demonstrated by using the IPA fields instead of their MC counterparts (open diamonds).

$$\delta_\tau(r) = 100\left\langle\frac{|\tau_{\mathrm{ipa}}(r; x) - \tau_{\mathrm{true}}(r; x)|}{\tau_{\mathrm{true}}(r; x)}\right\rangle (\%). \qquad (17)$$

At the smallest resolution ($r = \ell = 12.5$ m), we use the data in Fig. 5a as well as another realization of the same model; this yields $\delta_\tau(\ell) \approx 8\%$. The resolution is

then degraded by a factor of 2 and the retrieval/averaging procedure repeated in two ways:

1) "degrade-then-retrieve," which is what would happen if the detector's optics were different:

$$\tau_{ipa}(r; x) = \tau_{pp}\left[\frac{1}{r} \int_x^{x+r} I_{MC}(x') \, dx'\right]; \qquad (18a)$$

2) "retrieve-then-degrade," meaning that high-resolution radiance data is available but for some reason we only seek optical depths representative of larger scales:

$$\tau_{ipa}(r; x) = \frac{1}{r} \int_x^{x+r} \tau_{pp}[I_{MC}(x')] \, dx'. \qquad (18b)$$

After 10 coarse-graining steps ($r = L = 12.6$ km), a single radiance value is left to be compared with the average optical depth, $\langle\tau\rangle = 13$. Results are shown in Fig. 13b. Finally, the whole degrade-then-retrieve procedure is repeated with IPA radiances instead of MC ones; this guarantees than $\delta_\tau(\ell) \equiv 0$, followed by a steady error growth due to the increasing role of the concavity of $I_{pp}(\tau)$, hence convexity of $\tau_{pp}(I) = I_{pp}^{-1}(I)$. Indeed, Jensen's (1906) inequality $\langle\tau_{pp}(I)\rangle \geq \tau_{pp}(\langle I\rangle)$ becomes stronger since, as r increases, so does the subgrid variability.

As resolution is gradually degraded, there is no difference between the two methods at first when MC radiances are used because pixel-to-pixel increments are quite small (recall from Figs. 5b and 6 that this field is effectively differentiable). Both methods lead to an improvement in average retrieval error but a bifurcation occurs. The retrieve-then-degrade curve decreases monotonically whereas its degrade-then-retrieve counterpart starts increasing at $\approx$2-km scale ($\delta_\tau \approx 2\%$) and eventually reaches $\delta_\tau(L) \approx 12\%$, exceeding even the original pixel-scale error of 8%. By comparison with the results for IPA radiance, we see that the large-scale component to the retrieve-then-degrade error curve is traceable to the convexity of $\tau_{pp}(I)$. This large-scale error is closely related to Cahalan et al.'s (1994a) "plane-parallel bias," found to be 15%–20% for the difference between domain-averaged albedos for homogeneous and fractal clouds.

The radiative smoothing scale $\sqrt{\langle\rho^2\rangle} \approx 200$ m indicates roughly the inflection point of the monotonically decreasing retrieve-then-degrade error curve. Spatial averaging must be done up to this scale at least to reduce significantly the effects of pixel cross-talk. If plane-parallel theory is used to interpret remotely sensed data, there is no point in considering scales less than η_{rad} ($\approx$600 m in this case). Ignoring this will, in particular, lead to an underestimate of the small-scale variability of cloud properties. The accuracy of the retrieve-then-degrade method is excellent at the largest scale, achieving $\delta_\tau(L) \approx 0.3\%$. Discussing albedo prediction rather than optical depth retrieval, Cahalan et al. (1994b) refer

to this residual large-scale error due to horizontal fluxes as "IPA biases."

In essence, we have used a one-point statistic of a simple diagnostic $\tau_{ipa}(r; x)$, showing that its accuracy is contingent on the two-point statistic η_{rad}. Marshak et al. (1995) conduct a more detailed study of IPA breakdown using two-point multifractal statistics and propose an improved "nonlocal" IPA where the Gamma distribution in Eq. (13a) is interpreted as a smoothing (roughening) kernel in a convolution (deconvolution) product with the IPA prediction of I (retrieval of τ).

2) MULTICHANNEL RETRIEVAL OF $\langle\tau\rangle$, Δ_z, AND OTHER CLOUD PROPERTIES

Like any violation of a symmetry (in this case, scale invariance) in a physical system, the Landsat scale break can be used to extract information about the clouds. With a single image at visible wavelengths, empirical determination of η_{rad} puts constraints on the average optical thickness $\langle\tau\rangle$ and the geometrical cloud thickness Δ_z that prevail in the scene. To this effect, we can use either the analytical relation in Eq. (8) or its numerical counterpart in Fig. 10. For instance, in Figs. 1 and 2 we have $\eta_{rad} \approx 0.2$–0.3 km. Using the ratio in Eq. (15), we infer that $\sqrt{\langle\rho^2\rangle} \approx 0.1$–0.2 km; this value can be obtained by slightly decreasing Δ_z and/or increasing $\langle\tau\rangle$ with respect to our canonical values (respectively, 0.3 km and 13).

In conjunction with another TM channel, still dominated by multiple scattering, for the same scene a similar type of constraint is put on $\langle\tau'\rangle$ and Δ_z. Using plausible assumptions on the droplet-size distribution and Mie computations, we can obtain τ as a function of wavelength to within a proportionality constant; so we can solve for the three unknowns: $\langle\tau'\rangle$, $\langle\tau'\rangle$, and Δ_z. With a third channel, and already knowing the proportionality constant (hence $\langle\tau''\rangle$), we can access another cloud parameter, for example, effective droplet radius.

b. Active methods

Lidar observations are based on time-resolved returns from a pulsed laser on a ground-based, airborne, or satellite platform. In the simplest case, the signal is interpreted as a single scattering through 180°. The effects of multiple scattering are often corrected for, and even exploited to obtain, new information (cf. Flesia and Schwendimann 1995). However, the multiple scattering theory is generally developed in the small scattering-angle approximation that is sufficient when the detector's aperture is adjusted to the small linear size of the laser beam at the cloud's illuminated boundary. Focus on a single backscatter means that attenuation before and after the scattering event will limit penetration depth to a couple of photon MFPs, enough to probe aerosol and cirrus completely but only the first layers of clouds. For all practical purposes, the main applications of cloud

lidar are in cielometry and the retrieval of the phase water is in at cloud base, or cloud top, depending on the configuration.

1) LITE OBSERVATIONS OF MARINE Sc

The era of space-based atmospheric probing with lidar was open by the 1994 shuttle-based lidar-in-space technology experiment (LITE); its beam divergence and detector field-of-view (FOV) were standard, on the order of milliradians, leading to hundreds of meters at cloud level (Winker et al. 1996). Specifically, the beam was ≈ 0.3 km in diameter with a nighttime footprint of about 0.9 km.

Remarkably long return times ($t_R = \lambda/c$) were observed in the LITE data when low-altitude dense marine Sc were present (R. Menzies 1995, personal communication; D. Winker 1995, personal communication). More precisely, when the time-dependent return signal is interpreted as resulting from a single backscattering at a location determined by $\lambda/2$, then it seemed to occur sometimes from below sea level. For such clouds, we have $\Delta_z \approx 0.2$–0.4 km and altitudes around 1 km. To estimate the average (in-cloud) return time, we can use the data in Fig. 11 because $\sqrt{\langle \rho^2 \rangle}$ fall entirely within the detector's FOV; this yields $\langle \lambda \rangle / \Delta_z \approx 1.5$ (large τ) to ≈ 3 (small τ). However, as previously mentioned, we are dealing with rather broad λ distributions where total paths about $2(1 - g)\langle \tau \rangle$ times the mean $\langle \lambda \rangle$ will almost surely occur. Given the tenfold (approximately lognormal) natural variability of optical depth in marine Sc studied by Cahalan and Snider (1989), we predict λ / Δ_z ratios of up to 6 for $\langle \tau \rangle \approx 10$, 18 for $\langle \tau \rangle \approx 40$. In this case, $\lambda/2$ is indeed commensurate with cloud-base altitude and the detected PDF of $\lambda/2$ will certainly "unfold" into negative values.

The broad nature of the distribution of total in-cloud path is a key ingredient in our physical explanation of the expression for reflected spot size in Eq. (8). Therefore, its empirical validation with LITE observations provides an independent confirmation of the theoretical explanation we propose for the Landsat scale break based on horizontal photon diffusion.

2) NEW CONCEPTS IN CLOUD LIDAR

We see LITE as the forerunner of a whole new class of cloud lidar systems. In these systems the emphasis is shifted from single to multiple scattering, which means going from milliradian to radian FOVs if the cloud is at close range (i.e., ground based or airborne). There is only one foreseeable way to defeat the limitation imposed by the two-way exponential attenuation dictated by Bouger–de Beer's law in the standard lidar equation: collect the radiance that is (conservatively) scattered out of the laser beam wherever it reappears.

The basic theory of "wide-angle" lidar is the same as that developed in this study to explain the idiosyncratic Landsat and LITE phenomena that occur when dense clouds are observed: scale breaks and long tails, respectively. The idea is to remotely sample as best we can the spatial and temporal Green functions of the cloud to determine at least $\langle \rho^2 \rangle$ and $\langle \lambda \rangle$; in the former case, this calls for some form of imaging of the weak, highly scattered signal at relatively large distances from the beam, at least $\approx \sqrt{\langle \rho^2 \rangle}$. Assuming this can be achieved, the relations in Eqs. (8) and (11) (or, better still, Figs. 10–11) are then used to determine $\langle \tau \rangle$ and Δ_z at roughly $2\sqrt{\langle \rho^2 \rangle}$, namely, 0.5-km resolution. The technological challenge is, of course, the low-light imaging in potentially noisy environments; promising avenues are discussed by Davis et al. (1996c) for both spaceborne and ground-based configurations.

Recent advances in medical imaging in 3D are being based on "diffusing wave spectroscopy" (Yodh and Chance 1995), which is used to determine the position and size of pathological (IR-absorbing) entities such as aneurysms embedded in healthy (IR-scattering) tissue. It is noteworthy that wide-angle cloud lidar does a similar task for meteorology: detecting the presence of the cloud's nonilluminated boundary (that is, indeed, absorbing about half the photons) by scrutinizing the space–time return from a pulsed laser.

Finally, the differential between the Green functions of actual clouds and their theoretical counterparts predicted by plane-parallel theory will inform us about clouds' internal variability at scales below the nominal 0.5-km resolution for the determination of bulk properties: the (mean) optical and physical thicknesses. We recall that observational Green function analysis is standard procedure in the laboratory, primarily to determine the structure of the sample; for instance, coherent X-ray or neutron scattering patterns tell about the crystalline or amorphous microstructure of a sample in materials science. Wide-angle and spaceborne cloud lidar will therefore be timely additions to this long-standing scientific tradition.

7. Summary and discussion

We have addressed an ongoing issue concerning the statistical properties of cloudy Landsat scenes: what is the mechanism that produces the break observed in power-law behavior for the spatial wavenumber spectra $E_i(k)$ of the reflected radiance field? Specifically, we have $E_i(k) \sim k^{-\beta}$ with $\beta \sim 5/3$, as expected if the atmosphere's liquid water content is being advected by the turbulent horizontal wind field. However, for the largest observable k values corresponding to the smallest scales ($r = 1/k \lesssim \eta_{rad} \approx 0.2$–$0.4$ km), we invariably see a transition to smoother, even differentiable, fields with $\beta > 3$.

In previous explanations, the smoothing is either dismissed as an instrumental or statistical artifact (Lovejoy et al. 1993), or predicted to occur at the scale of the cloud's physical thickness Δ_z or else at a scale commensurate with the "transport" mean free path l_t (Ca-

halan and Snider 1989). We recall that photons, after propagation over one transport mean free path, have suffered enough scatterings to essentially "forget" their original position and direction. We have presented numerical and analytical arguments showing that the smoothing is real and occurs at a scale commensurate with the harmonic mean of Δ_z and l_t. The smoothing scale η_{rad} automatically puts an absolute lower bound on the domain of applicability of cloud parameter retrieval schemes that depend on standard plane-parallel theory, in other words, an operational "independent pixel" approximation.

By invoking elementary Green function theory, we have shown that the physical interpretation of the Landsat scale break is essentially the extent that solar photons can diffuse horizontally (by way of multiple scattering) from impact to escape at cloud top. By the same token, we explain the recent observation of unexpectedly long pulse stretching in returns from marine stratocumulus during LITE, the first spaceborne lidar experiment, by multiple scattering in the diffusion approximation. Armed with a physical understanding of the scale break, we sketched both passive and active cloud remote sensing methodologies that yield both optical and geometrical thicknesses of stratiform clouds.

Other forms of atmospheric radiative smoothing have been investigated previously, generally of a milder kind than discussed here. One well-explored line of research in coherent optics is the distortion of a planar wave front by atmospheric turbulence, leading to the spreading of stellar images (e.g., Tatarski 1961). The community invested in remote sensing of the earth's surface (indeed Landsat's original application) is interested in another type of radiative smoothing: observation of a variable ground albedo field through a thin homogeneous atmosphere (Odell and Weinman 1975; Otterman and Fraser 1979; Tanré et al. 1981; Royer et al. 1989; among others). One of the most mathematically sophisticated treatments of this problem is Diner and Martonchik's (1984a,b) use of horizontal Fourier transforms of the radiance field. Their approach was generalized by Stephens (1986) to include horizontal variability of the optical properties of the atmosphere. Stephens (1988a) uses this general full matrix solution of the discretized 3D radiative transfer equation to demonstrate how even a single oscillation in the optical depth field excites all the higher-frequency radiance modes, hence net horizontal fluxes, through the coupling in the extinction (sink) term and multiple scattering (source) term. From Stephens's standpoint, the Landsat scale break is a damping of the highest Fourier radiance modes, traceable in all likelihood to the enhancement at a specific scale of the matrix coefficients related to multiple scattering.

Small-scale upwelling radiances are relevant primarily to remote sensing, whereas large-scale vertical fluxes are the important quantities in atmospheric radiative budget computations; in particular, subgrid parameter-izations of solar heating rates in GCMs depend on these fluxes. Stephens (1988b) develops a simple parameterization of his general Fourier-mode coupling scheme to assess the overall effect of spatial variability on albedo, transmittance, and absorptance. In a sequel to this study, we also switch our attention from radiance to flux measurements, in particular to predict the magnitude of net horizontal fluxes in marine stratocumulus and assess the impact they have on estimates of total absorption in the atmospheric column.

APPENDIX

Scale-Invariant Cloud Models Used in This Study

In this paper we use stochastic models to mimic the natural fluctuations of cloud optical depth. The analyses of Davis et al. (1994, 1996a) and Marshak et al. (1996, manuscript submitted to *J. Atmos. Sci.*) of LWC fluctuations inside marine Sc during FIRE and ASTEX support the use of scale-invariant (or simply "fractal") models that obey power law statistics over at least three orders of magnitude in scale. For FIRE, scaling is observed down to $\approx$20–40 m, roughly the Landsat pixel scale. In this appendix, we use multiplicative cascades to obtain models with scale-invariant properties.

Starting with a homogeneous slab of length L, one transfers a fraction f_1 of the mass from one half to the other in a randomly chosen direction. This is equivalent to multiplying the originally uniform density field on either side by factors $W_1^{(\pm)} = 1 \pm f_1$. The same procedure is repeated recursively at ever smaller scales using fractions f_i ($i = 2, 3, \cdots$) on segments of length r_{i-1}, where

$$r_n = \frac{L}{2^n}. \tag{A1}$$

a. Singular cascades

We now parameterize the multiplicative weights as

$$W_i^{(\pm)} = 1 \pm (1 - 2p)$$

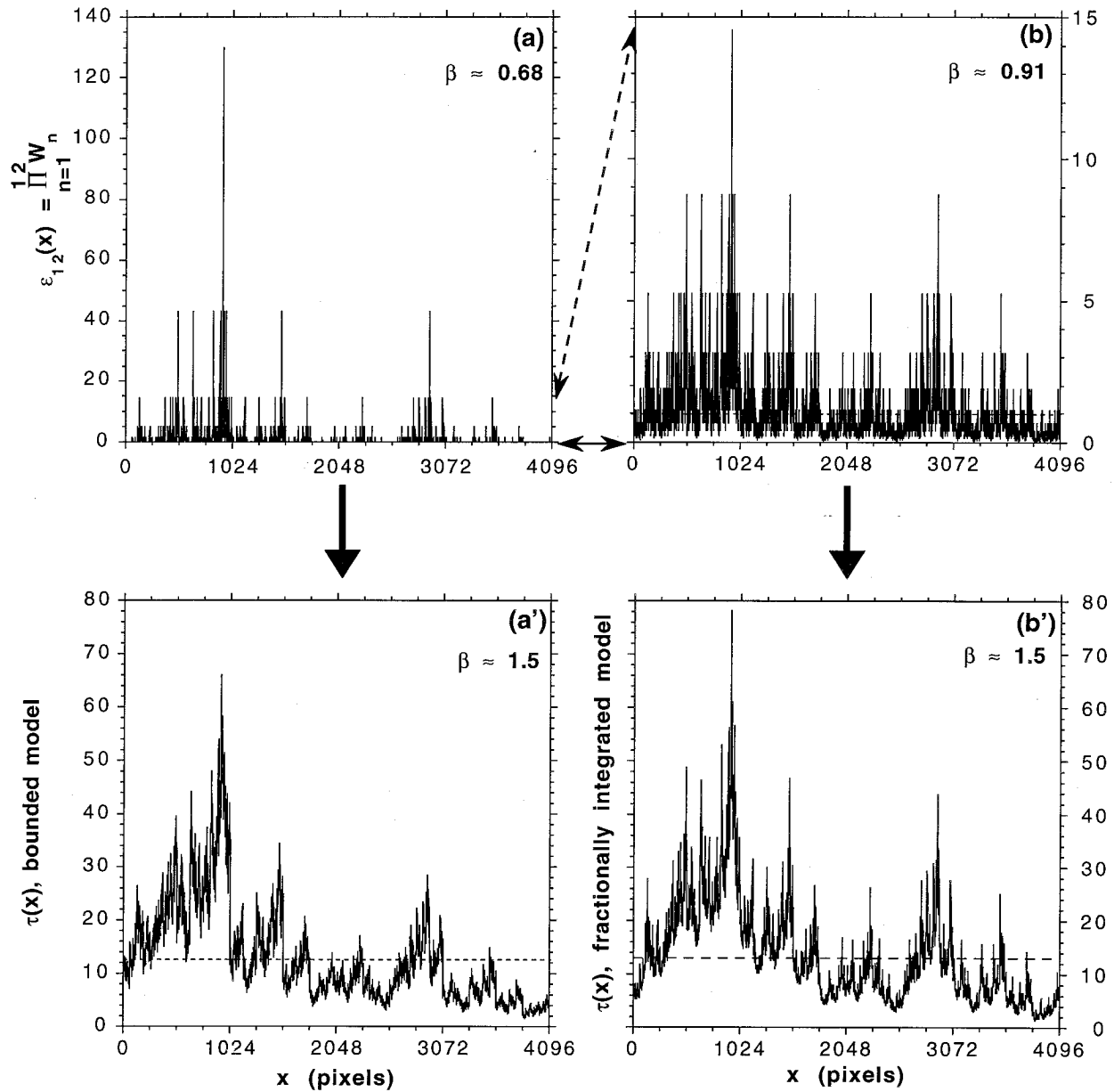$$= \begin{cases} 2p \\ 2(1 - p) \end{cases}, \quad 0 \le p \le 1/2, \tag{A2}$$

FIG. A1. Random singular cascade models and associated scale-invariant optical depth fields. Two multiplicative "p-model" cascades with unit mean and using the same sequence of pseudo-random numbers, $n = 12$ cascade steps, and respectively (a) $p = 0.25$, (b) $p = 0.375$ in Eq. (A2). (a') Twelve-step bounded cascade model modified from the case in panel (a) using Eq. (A5) with $H = 1/3$. (b') The singular cascade model in panel (b) after fractional integration with $H^* = 0.29$ in Eq. (A7) and a linear transformation. Parameters were tuned so that the data in both lower panels have the same mean $\langle \tau \rangle = 13$, variance in $\log_{10}\tau \approx 0.2$, and spectral exponent $\beta_\tau = 1.5$.

independently of i, with 50/50 probability for the signs. This leads to multifractal "p models," originally proposed by Meneveau and Sreenivasan (1987) to simulate the highly intermittent spatial fluctuations of the kinetic energy dissipation in turbulence. In this primarily tutorial model, constant fields, $E_\epsilon(k) \propto \delta(k)$, are retrieved in the limit $p \to 1/2^-$ and randomly positioned Dirac δ's for $p = 0$. So p directly controls the degree of concentration of the E-field at each cascade step. The spectral exponent defined in $E_\epsilon(k) \sim 1/k^{\beta_\epsilon}$, $k > 0$ is

$$0 \le \beta_\epsilon(p) = 1 - \log_2[1 + (1 - 2p)^2] < 1. \text{ (A3)}$$

Figures A1a,b show examples with $p = 0.250, 0.375$ (hence $\beta_\epsilon = 0.68 \cdots , 0.91 \cdots$), respectively, for $n = 12$, hence a total of 4096 points.

The intense spikiness we see in Figs. A1a,b is witness to the singularity of the model; in the limit $n \to \infty$, we do not even obtain a "function" of $x \in [0, L)$ in the traditional sense of the word. Indeed, the product $\epsilon(x) = \Pi_1^\infty W_i$ vanishes with probability one, since, for $n \gg 1$, we have

$$\ln \epsilon_n(x) = \ln \prod_1^n W_i$$

$$= \sum_1^n \ln W_i$$

$$= \sum_1^n \ln[1 \pm (1 - 2p)];$$

hence

$$\langle \ln \epsilon_n(x) \rangle \approx \frac{n}{2} \sum_\pm \ln[1 \pm (1 - 2p)] \qquad \text{(A4)}$$

$$= n \ln[2\sqrt{p(1-p)}] \rightarrow -\infty,$$

for $0 \le p < 1/2$, as $n \rightarrow \infty$. Yet the spatial average is maintained at unity by construction; so, $\epsilon_n(x) \rightarrow +\infty$ just often and/or just fast enough to counteract the drift in Eq. (A4). This type of model is best viewed as a "measure" or "generalized" function (in the sense of Schwartz), namely, a mathematical entity defined only under integrals. The prime examples are Dirac's (generalized) δ functions, obtained here for $p = 0$, hence $\beta_\epsilon = 0$ in Eq. (A3).

Since $\beta_\epsilon < 1$ in Eq. (A3), Davis et al. (1996a) would classify $\epsilon(x)$ as a stationary process: arbitrarily large jumps are allowed, so that the process can have at once large deviations, sometimes misleadingly associated with stationarity violation, and resume modal (i.e., most frequent) values very fast. In other words, spatial correlations as defined by $\langle \epsilon(x)\epsilon(x + r) \rangle$, the Fourier dual of $E_\epsilon(k)$, are very short ranged.

In summary, singular cascade models have interesting intermittency properties, but their spectra with $\beta_\epsilon < 1$ do not scale as observed optical depth fields that invariably have $\beta_\tau > 1$.

b. Bounded cascades

A simple way to obtain $\beta_\tau > 1$ is to reduce the variance of the multiplicative weights in Eq. (A2) at each cascade step. Taking

$$W_i^{(\pm)} = 1 \pm (1 - 2p)r_i^H{}_{-1},$$

$$0 \le p < 1/2, \qquad H > 0, \qquad \text{(A5)}$$

leads to Cahalan et al.'s (1990, 1994a) "bounded" cascade models. Figure A1a′ shows the bounded version of the p model in Fig. A1a. The limit $H \rightarrow \infty$ yields a single jump (Heaviside step) from $2p$ to $2(1 - p)$ at $x = L/2$.

By reducing the size of the jumps as the scale decreases, we are obviously introducing a degree of continuity into the model. Consequently, it takes a relatively long time to cumulate large deviations; in turn, this means that the two-point correlations become long ranged. Accordingly, these models are patently nonstationary, having

$$1 < \beta_\tau(H) = \min\{2H, 1\} + 1 \le 2, \qquad \text{(A6)}$$

independent of p (Marshak et al. 1994); this simple theoretical result, however, applies strictly at $n = \infty$; for $n = 12$, $H = 1/3$ and $p = 0.25$ yield $\beta_\tau \approx 1.5$ rather than 5/3. The more interesting function of p is to modulate the prefactor in the power law wavenumber spectrum; in other words, it controls the overall one-point variance of the model (Cahalan et al. 1994a).

Marshak et al. (1994) investigated the higher-order two-point statistics of these models that prove to be multifractal in the sense that their characterization calls for an infinite number of exponents. This adds to the realism of bounded cascades as cloud models because the fluctuations of liquid water density inside marine Sc are multifractal (Davis et al. 1994, Marshak et al. 1997, manuscript submitted to *J. Atmos. Sci.*). Stochastic cloud models are frequently developed first in one spatial dimension, and bounded cascades are not an exception. So extension into higher dimensions is another asset; in this case, see Callahan (1994) and Davis et al. (1996b) for the details in 2D.

c. Fractional integration

Another way of transforming the stationary situation described in section Aa (singular cascades with $\beta_\epsilon < 1$) into a more realistic nonstationary one ($\beta_\tau > 1$) is suggested by Schertzer and Lovejoy (1987): power law filtering in Fourier space will bring the spectral exponent to any prescribed value. In particular, we can have

$$\beta_\tau(p, H^*) = \beta_\epsilon(p) + 2H^*, \qquad \text{(A7)}$$

where H^* describes the low-pass filter in $1/k^{H^*}$. In physical space, this operation—also known as "fractional integration" (e.g., Pearson 1990)—is a convolution with a weakly singular kernel that brings measures into the realm of functions, finite at almost every point. By now, jumps are quite small because $\epsilon(x)$ generally is vanishingly small for most values of x. Here again, we have introduced (stochastic) continuity; accordingly, two-point correlations have become long ranged.

Figure A1b′ shows the result for $\epsilon(x)$ in Fig. A1b ($\beta_\epsilon \approx 0.9$) when we require $\beta_\tau \approx 1.5$ by setting $H^* = 0.3$ in Eq. (A7). The proportionality factor in the power law filter used to produce this particular optical depth field was set to give the same mean τ and variance in $\log_{10}\tau$ as in Fig. A1a. This means that the two $\tau(x)$ fields will have nearly the same $\sigma_\tau/\langle\tau\rangle$ and hence, according to Cahalan (1994), the same domain-average albedo.

Being multifractal with at least one more tunable parameter than bounded cascades, linearly transformed fractionally integrated singular cascades are good candidates for simulating observed liquid water fluctuations (Davis et al. 1996b). Furthermore, they generalize easily to higher dimensions (Wilson et al. 1991).

d. Universality with respect to radiative smoothing

Marshak et al. (1995) argue that the universality class defined by the occurrence of small-scale radiative smoothing is quite vast, including those discussed above and many more. There seem to be only two important conditions. One is structural and the other is radiative:

1) the cloud model is stochastically continuous and
2) photon transport is dominated by diffusion-type multiple scattering.

For scale-invariant fields, property 1) follows from $\beta_\tau > 1$ that is ubiquitous in cloud liquid water fluctuations, starting with King et al. (1981) airborne probings. Furthermore, we believe that, given condition 1), condition 2) is fulfilled as soon as the mean optical thickness is large enough, and from there follows our basic result in Eq. (8) of the main text. Whatever it is, "large enough" seems to be often the case in nature since many of King et al. (1990) radiance measurements inside marine stratocumulus display the characteristics of diffusion.

Davis (1992) has documented a number of counter examples, optically thick scale-invariant media where diffusion and linear transport theory disagree, but they all have $\beta_\tau < 1$ and are more representative of broken cloud than stratus.

REFERENCES

Barker, H. W., and J. A. Davies, 1992: Cumulus cloud radiative properties and the characteristics of satellite radiance wavenumber spectra. *Remote Sens. Environ.,* **42,** 51–64.

Cahalan, R. F., 1989: Overview of fractal clouds. *Advances in Remote Sensing Retrieval Methods,* A. Deepak, H. Fleming, and J. Theon Eds., Deepak, 371–389.

——, 1994: Bounded cascade clouds: Albedo and effective thickness. *Nonlinear Proc. Geophys.,* **1,** 156–165.

——, and J. H. Joseph, 1989: Fractal statistics of cloud fields. *Mon. Wea. Rev.,* **117,** 261–272.

——, and J. B. Snider, 1989: Marine stratocumulus structure. *Remote Sens. Environ.,* **28,** 95–107.

——, M. Nestler, W. Ridgway, W. J. Wiscombe, and T. L. Bell, 1990: Marine stratocumulus spatial structure. *Proc. Fourth Int. Meeting on Statistical Climatology,* Wellington, New Zealand, New Zealand Meteor. Service, 28–32.

——, W. Ridgway, W. J. Wiscombe, T. L. Bell, and J. B. Snider, 1994a: The albedo of fractal stratocumulus clouds. *J. Atmos. Sci.,* **51,** 2434–2455.

——, ——, ——, S. Gollmer, and Harshvardhan, 1994b: Independent pixel and Monte Carlo estimates of stratocumulus albedo. *J. Atmos. Sci.,* **51,** 3776–3790.

Case, K. M., and P. F. Zweifel, 1967: *Linear Transport Theory.* Addison-Wesley, 342 pp.

Corssin, S., 1951: On the spectrum of isotropic temperature fluctuations in isotropic turbulence. *J. Appl. Phys.,* **22,** 469–473.

Davis, A., 1992: Radiation transport in scale-invariant optical media. Ph.D. thesis, McGill University, 325 pp. [Available from McGill University, 47 Sherbrooke St. West, Montreal, PQ H3A 3N6, Canada.]

——, and A. Marshak, 1996: Cloud responses from CW and pulsed lasers as Green functions: What do they tell us? and Can we measure them? *Proc. Eighth Int. Workshop on Multiple Scattering Lidar Experiments (MUSCLE 8),* Defense Research Establishment Valcartier, Québec PQ, Canada, 67–71.

——, S. Lovejoy, and D. Schertzer, 1993: Supercomputer simulation of radiative transfer inside multifractal cloud models. *IRS'92: Current Problems in Atmospheric Radiation,* S. Keevallik and O. Kärner, Eds., Deepak, 112–115.

——, A. Marshak, W. J. Wiscombe, and R. F. Cahalan, 1994: Multifractal characterizations of nonstationarity and intermittency in geophysical fields, observed, retrieved or simulated. *J. Geophys. Res.,* **99,** 8055–8072.

——, ——, ——, and ——, 1996a: Scale-invariance of liquid water distributions in marine stratocumulus. Part I: Spectral properties and stationarity issues. *J. Atmos. Sci.,* **53,** 1538–1558.

——, ——, ——, and ——, 1996b: Multifractal characterizations of intermittent and nonstationary geophysical signals—A model-based perspective on ergodicity issues illustrated with cloud data. *Current Issues in Nonstationary Analysis (Proceedings of the 2nd International Worskshop on Nonstationary Processes and their Applications),* G. Treviño, J. Hardin, B. Douglas, and E. Audreas, Eds., World Scientific, 97–158.

——, D. Winker, A. Marshak, J. D. Spinhine, R. F. Cahalan, S. Love, S. H. Melfi, and W. J. Wiscombe, 1996c: Retrieval of physical and optical cloud thicknesses from space-borne and wide-angle lidar. *Advances in Atmospheric Remote Sensing with Lidar,* R. Neuber, P. Rairoux, and A. Ansmann, Eds., Springer-Verlag.

Diner, D. J., and J. V. Martonchik, 1984a: Atmospheric transfer of radiation above an inhomogeneous non-Lambertian ground, 1—Theory. *J. Quant. Spectrosc. Radiat. Transfer,* **31,** 97–125.

——, and ——, 1984b: Atmospheric transfer of radiation above an inhomogeneous non-Lambertian ground, 2—Computational considerations and results. *J. Quant. Spectrosc. Radiat. Transfer,* **32,** 279–304.

Flesia, C., and P. Schwendimann, Eds., 1995: Special section on multiple scattering in lidar experiments (MUSCLE). *Appl. Phys. B: Lasers Opt.,* **B60,** 315–362.

Gollmer, S. M., Harshvardan, R. F. Cahalan, and B. Wielicki, 1994: Observed scale-break in marine stratocumulus power spectrum from Landsat thematic mapper data. *Eos, Trans. Amer. Geophys. Union,* **75** (Suppl.), 92.

Harshvardan, B. A. Wielicki, and K. M. Ginger, 1994: The interpretation of remotely sensed cloud properties from a model parameterization perspective. *J. Climate,* **7,** 1987–1998.

Henyey, L., and J. Greenstein, 1941: Diffuse radiation in the galaxy. *Astrophys. J.,* **93,** 70–83.

Jensen, J. L. W. V., 1906: Sur les fonctions convexes et les inegalités entre les valeurs moyennes. *Acta Math.,* **30,** 789–806.

King, M. D., L. F. Radke, and P. V. Hobbs, 1990: Determination of the spectral absorption of solar radiation by marine stratocumulus clouds from airborne measurements within clouds. *J. Atmos. Sci.,* **47,** 894–907.

King, W. D., C. T. Maher, and G. A. Hepburn, 1981: Further performance tests on the CSIRO liquid water probe. *J. Atmos. Sci.,* **38,** 195–200.

Kraichnan, R. H., 1967: Inertial ranges in two-dimensional turbulence. *Phys. Fluids,* **10,** 1417–1423.

Lovejoy, S., 1982: Area–perimeter relation for rain and clouds areas. *Science,* **216,** 185–187.

——, D. Schertzer, P. Silas, Y. Tessier, and D. Lavallée, 1993: The unified scaling model of atmospheric dynamics and systematic analysis of scale invariance in cloud radiances. *Ann. Geophys.,* **11,** 119–127.

Marchuk, G., G. Mikhailov, M. Nazaraliev, R. Darbinjan, B. Kargin, and B. Elepov, 1980: *The Monte Carlo Methods in Atmospheric Optics.* Springer-Verlag, 208 pp.

Marshak A., A. Davis, R. Cahalan, and W. Wiscombe, 1994: Bounded cascade models as nonstationary multifractals. *Phys. Rev. E.; Stat. Phys. Plasmas Fluids Relat. Interdiscip Top.,* **49,** 55–69.

——, ——, W. J. Wiscombe, and R. F. Cahalan, 1995: Radiative smoothing in fractal clouds. *J. Geophys. Res.,* **100,** 26 247–26 261.

——, ——, ——, and ——, 1997: Scale invariance of liquid water

distributions in marine stratocumulus. Part II: Multifractal properties and intermittency issues. *J. Atmos. Sci.,* in press.

Meneveau, C., and K. R. Sreenivasan, 1987: Simple multifractal cascade model for fully developed turbulence. *Phys. Review Lett.,* **59,** 1424–1427.

Monin, A. S., and A. M. Yaglom, 1975: *Statistical Fluid Mechanics.* Vol. 2. MIT Press, 683 pp.

Obukhov, A., 1949: Structure of the temperature field in a turbulent flow. *Izv. Akad. Naut. SSSR, Ser. Geogr. I Geofiz.,* **13,** 55–69.

Odell, A. P., and J. A. Weiman, 1975: The effect of atmospheric haze on images of the earth's surface. *J. Geophys. Res.,* **80,** 5035–5040.

Otterman, J., and R. S. Fraser, 1979: Adjacency effects on imaging by surface reflection and atmospheric scattering: Cross radiance zenith. *Appl. Opt.,* **18,** 2852–2860.

Pearson, C. E., Ed., 1990: *Handbook of Applied Mathematics—Selected Results and Methods.* 2d ed. Van Nostrand Reinhold, 1307 pp.

Royer, A., A. Davis, and N. O'Niell, 1989: Analyse des effets atmosphériques dans les images HRV de SPOT. *Can. J. Remote Sens.,* **14,** 80–91.

Schertzer, D., and S. Lovejoy, 1987: Physical modeling and analysis of rain clouds by anisotropic scaling multiplicative processes. *J. Geophys. Res.,* **92,** 9693–9714.

Sèze, G., and L. Smith, 1990: On the dimension of cloud boundaries. *Proc. Seventh Conf. on Atmospheric Radiation,* San Francisco, CA, Amer. Metor. Soc., 47–57.

Stamnes, K., S.-C. Tsay, W. J. Wiscombe, and K. Jayaweera, 1988: Numerically stable algorithm for discrete-ordinates-method radiative transfer in multiple scattering and emitting layered media. *Appl. Opt.,* **27,** 2502–2512.

Stephens, G. L., 1986: Radiative transfer in spatially heterogeneous, two-dimensional anisotropically scattering media. *J. Quant. Spectrosc. Radiat. Transfer,* **36,** 51–67.

——, 1988a: Radiative transfer through arbitrarily shaped media. Part I: General solution. *J. Atmos. Sci.,* **45,** 1818–1835.

——, 1988b: Radiative transfer through arbitrarily shaped media. Part II: Group theory and closures. *J. Atmos. Sci.,* **45,** 1836–1838.

Tanré, D., M. Herman, and P. Y. Deschamps, 1981: Influence of the background contribution upon space measurements of ground reflectance. *Appl. Opt.,* **20,** 3676–3684.

Tatarski, V. I., 1961: *Wave Propagation in a Turbulent Medium.* R. A. Silverman, Transl., McGraw Hill, 285 pp.

Welch, R. M., and B. A. Wielicki, 1986: Cumulus cloud properties derived using Landsat data. *J. Climate Appl. Meteor.,* **25,** 261–276.

——, K. S. Kuo, B. A. Wielicki, S. K Sengupta, and L. Parker, 1988: Marine stratocumulus cloud fields off the coast of Southern California observed by Landsat imagery. Part I: Strutural characteristics. *J. Appl. Meteor.,* **27,** 341–362.

Wilson, J., D. Schertzer, and S. Lovejoy, 1991: Continuous multiplicative cascade models of rain and clouds. *Scaling, Fractals and Non-Linear Variability in Geophysics,* D. Schertzer and S. Lovejoy, Eds., Kluwer, 185–207.

Winker, D., R. H. Couch, and M. P. McCormick, 1996: An overview of LITE: NASA's Lidar In-space Technology Experiment. *Proc. IEEE,* **84,** 164–180.

Yodh, A., and B. Chance, 1995: Spectroscopy/imaging with diffusing light. *Phys. Today,* **48,** 34–40.